Superpixel segmentation for analysis of hyperspectral data sets, with application to Compact Reconnaissance Imaging Spectrometer for Mars data, Moon Mineralogy Mapper data, and Ariadnes Chaos, Mars

Martha S. Gilmore,[1] David R. Thompson,[2] Laura J. Anderson,[1] Nader Karamzadeh,[2] Lukas Mandrake,[2] and Rebecca Castaño[2]

Received 19 October 2010; revised 30 March 2011; accepted 14 April 2011; published 12 July 2011.

[1] We present a semiautomated method to extract spectral end-members from hyperspectral images. This method employs superpixels, which are spectrally homogeneous regions of spatially contiguous pixels. The superpixel segmentation is combined with an unsupervised end-member extraction algorithm. Superpixel segmentation can complement per pixel classification techniques by reducing both scene-specific noise and computational complexity. The end-member extraction step explores the entire spectrum, recognizes target mineralogies within spectral mixtures, and enhances the discovery of unanticipated spectral classes. The method is applied to Compact Reconnaissance Imaging Spectrometer for Mars (CRISM) images and compared to a manual expert classification and to state-of the-art image analysis techniques. The technique successfully recognizes all classes identified by the expert, producing spectral end-members that match well to target classes. Application of the technique to CRISM multispectral data and Moon Mineralogy Mapper (M^3) hyperspectral data demonstrates the flexibility of the method in the analysis of a range of data sets. The technique is then used to analyze CRISM data in Ariadnes Chaos, Mars, and recognizes both phyllosilicates and sulfates in the chaos mounds. These aqueous deposits likely reflect changing environmental conditions during the Late Noachian/Early Hesperian. This semiautomated focus-of-attention tool will facilitate the identification of materials of interest on planetary surfaces whose constituents are unknown.

Citation: Gilmore, M. S., D. R. Thompson, L. J. Anderson, N. Karamzadeh, L. Mandrake, and R. Castaño (2011), Superpixel segmentation for analysis of hyperspectral data sets, with application to Compact Reconnaissance Imaging Spectrometer for Mars data, Moon Mineralogy Mapper data, and Ariadnes Chaos, Mars, *J. Geophys. Res.*, *116*, E07001, doi:10.1029/2010JE003763.

1. Introduction

[2] Hyperspectral (hundreds of spectral bands) imaging spectrometers have now orbited 4 planets and our Moon. These instruments yield unprecedented information about atmospheric and ocean properties, surface mineralogy, and land cover characteristics of the Earth and planets. These rich data sets have spurred the development of a number of techniques for spectral classification. The goal of these techniques is to recover and recognize target materials from within spectra, but a number of issues make this task challenging. Hyperspectral data are affected by scene-specific noise both from the sensor itself and from transient atmospheric phenomena. The magnitude and nature of this noise is very difficult to anticipate, define, and therefore mitigate. Furthermore, planetary surfaces are often mixtures of materials resulting in spectra of mixed surface materials. For simplicity this mixing is often (reasonably) modeled as linear, but there are numerous cases where this assumption fails (e.g., the effect of dark materials in a mixed spectrum) [*Clark*, 1999]. Planetary regoliths, in particular, often include a pervasive component (e.g., Martian dust or dark asteroid surfaces created by space weathering) that contributes strongly to resulting spectra, masking target materials.

[3] Extraterrestrial planets present other unique challenges. Without the benefit of field verification, planetary surface compositions are potentially unconstrained. Planets may also contain materials that are not represented in spectral libraries, including minerals that are rare or metastable on Earth (e.g., reduced lunar minerals, dry Mars minerals, impact glasses). This leaves potential targets or anomalies undiscovered because they or their signatures were not expected. Techniques that are able to explore and characterize an entire spectral data set in an unbiased manner are desirable to search for novel mineralogy.

[4] Data analysis techniques also benefit mission operations. For example, due to data downlink restrictions, the

[1]Department of Earth and Environmental Sciences, Wesleyan University, Middletown, Connecticut, USA.
[2]Jet Propulsion Laboratory, California Institute of Technology, Pasadena, California, USA.

0148-0227/11/2010JE003763

Compact Reconnaissance Imaging Spectrometer for Mars (CRISM) instrument aboard the Mars Reconnaissance Orbiter (MRO) operates in two modes: (1) a global survey mode at reduced spatial and spectral resolution and (2) a high-resolution mode estimated to cover just ~5% of the planet at full spatial and spectral resolution. As many high-priority targets are selected opportunistically in response to analyzed survey images, complete and fast interpretation is vital for effective mission planning. However, manually hunting for particular mineralogical signatures is laborious and the volume of downlinked data may outpace the capacity for timely analysis. It is imperative that all survey data be analyzed robustly and rapidly to assist in tactical mission planning and identifying future targets during the finite lifetime of a planetary mission.

[5] We address the task of hyperspectral search and survey in planetary data sets where scene constituents are unknown. Specifically, we seek to design a semiautomated "focus of attention" tool to triage the data, assisting analysts by localizing salient materials and calling out distinctive regions for manual study. Our method uses a superpixel segmentation to reduce noise inherent in planetary data sets. Geometric analyses of the superpixel spectra are then used to identify end-member materials across a scene. We evaluate the performance of this process to identify relevant geologic materials in CRISM and Moon Mineralogy Mapper (M^3) data and apply it to the study of Ariadnes Chaos, Mars.

1.1. Current Practice for Mineralogical Search

[6] Two common data exploration strategies include classification with training examples and end-member detection algorithms.

1.1.1. Supervised Classification

[7] In order to find specific anticipated materials, analysts can classify new image pixels based on library spectra or training examples from similar data. Common classification approaches involve spectral angle projections onto known library samples or statistical classification based on methods using statistical and machine learning approaches [*Tso and Mather*, 2009]. This latter group includes decision trees [*Friedl and Brodley*, 1997] and kernel methods such as support vector machines [*Melgani and Bruzzone*, 2004]. Achieving good generalization performance on a new scene is difficult because imaging conditions and substrate may differ from the training examples. Such changes can easily overwhelm a subtle absorption band.

[8] Analysts seeking specific mineralogy often create color maps from chosen bands or band ratios in order to emphasize the key spectral features. This approach is ubiquitous in planetary science investigations and is typified by the CRISM summary products [*Pelkey et al.*, 2007; *Ehlmann et al.*, 2009; *Roach et al.*, 2009; *Salvatore et al.*, 2009]. Here, specific absorption bands associated with materials of interest are identified and used to compute summary values such as continuum-ratioed band depths or spectral slopes. These summary products are valuable guides for mineralogical search because they are immediately interpretable and may be minimally influenced by certain noise artifacts or image variability. For Earth and planetary data sets, the expert system Tetracorder [*Clark et al.*, 2003] uses expert-defined rules to integrate library spectrum fits and absorption features for automated mapping and classification.

[9] These techniques are effective for mapping scenes with known mineralogy. However, unconstrained mineralogical searches in new images are difficult and require considerable user expertise. All supervised techniques are hindered by their inability to find materials that are not anticipated. Moreover, confirmation of mineralogical species remains labor intensive. A common approach is to manually identify pixels with the highest index values and average them to reduce both instrument and atmospheric noise and produce a spectrum that is more readily interpretable by comparison to spectral libraries. Here we provide a technique that combines and unsupervised classification with noise reduction using superpixels to efficiently assess and display the spectral variability of an image cube.

1.1.2. Hyperspectral Search With End-Member Detection

[10] Observed reflectance at visible/near infrared wavelengths is generally understood to be the combination, possibly linear, of a smaller set of "end-member" spectra. These individual constituents need not be present as pure spectra in the scene. While identifying the spectral end-members is essential for hyperspectral unmixing and abundance estimation, it can also be informative for hyperspectral search as the end-member spectra presumably represent the purest examples of all the distinctive materials that are present. Confounding factors include instrument noise, atmospheric effects, and substrate variability, each of which may introduce additional spectral variants of otherwise identical minerals. Mature end-member detection algorithms aim to locate distinctive materials despite these confounding factors.

[11] A wide range of end-member detection algorithms exists for both linear and nonlinear mixing models [e.g., *Parente and Bishop*, 2010]. Typical *geometric* end-member detection approaches leverage the geometric properties of the linear mixing model, in which end-member spectra are vertices of a high-dimensional (determined by the spectral resolution) simplex enclosing the data. Typical examples include N-FINDR [*Winter*, 2004], Vertex Component Analysis [*Nascimento and Bioucas-Dias*, 2005], or the Sequential Maximum Angle Convex Cone (SMACC) method used in this work [*Gruninger et al.*, 2004]. The Pixel Purity Index [*Boardman et al.*, 1995] is a measure of a pixel's "extremity" with respect to the other data points in the image, and can be used for end-member detection through an iterative, manually guided process. Alternatively, *statistical* end-member detection methods analyze the distribution for the data with end-member spectra as unknown parameters, and estimate these using statistical techniques [*Dobigeon et al.*, 2009]. Other previous approaches for unsupervised spectral analysis use statistical properties of the data. *Marzo et al.* [2006] apply a general k-means clustering strategy to Thermal Emission Spectrometer data and recover geologically meaningful categories. Later work uses clustering for intelligent compression of high-volume images [*Marzo et al.*, 2008]. *Roush and Hogan* [2007] and *Hogan and Roush* [2009] analyze catalogs of infrared spectra collected in the laboratory; they propose a self-organizing map (SOM) to learn a low-dimensional manifold where clusters better represent the key spectral variations. In each case, the learned representations define class categories that can then label new spectra [*Marzo et al.*, 2009]. Cluster centroids correspond to representative mineral types; they do not generally include

the purest samples or spectral anomalies. Such methods are of particular interest where the linear mixing model does not hold or where one wishes class categories to follow the statistical distribution of the data.

[12] Automatic end-member detection is well suited for mineralogical search in planetary data sets because it is not necessary to know the constituent spectra in advance. This increases the likelihood of detecting novel minerals that are highly mixed or present in subtle quantities in intimate mixture. Despite a growing body of research on the topic, cited use of automated end-member detection for planetary data sets is relatively rare [*Parente and Bishop*, 2010]. Most currently cited methods for end-member detection are sensitive to any noise or instrument artifacts present in even one pixel thus requiring extensive data cleaning. Unfortunately, subtle absorption features near the level of noise would then be erased. These algorithmic limitations have largely precluded automated end-member detection in what would otherwise be a natural application.

[13] The following section presents a new approach for applying end-member detection techniques to superpixel representations of a given hyperspectral image. To our knowledge no prior effort has used superpixels to describe hyperspectral data. This new image representation leverages *spatial* relationships to reduce noise while preserving key spectral features. Several previous studies have demonstrated using spatial information to improve end-member extraction [*Plaza et al*., 2002; *Zortea and Plaza*, 2009; *Zhang et al.* 2008; *Rogge et al.*, 2007]. Superpixel representations are a new instance of this strategy, and can potentially make automated end-member analysis more relevant for planetary data sets.

2. Methods

[14] Broadly speaking our method consists of two stages: an initial *superpixel segmentation* for noise reduction followed by end-member detection to identify salient minerals. The two together are complementary: the first analyzes local pixel relationships spatially and spectrally, while the second performs a scene-wide statistical analysis on the resulting spectra. Here we describe each step in detail and the techniques for evaluating the resulting detections for "focus of attention" cues in mineralogical search.

2.1. Image Data Sets

[15] The CRISM imaging spectrometer aboard MRO acquires data over the 362–3920 nm spectral range. The instrument includes two separate detectors that acquire light over the 362–1053 nm range (S detector) and the 1002–3920 nm range (L detector). CRISM collects data in two primary modes: a high-resolution targeted mode and a multispectral survey mode [*Murchie et al.*, 2007a]. The full-resolution target (FRT) images acquire 544 wavelength channels over a ~10 × 10 km area at ~18 m/pixel. For this work, we utilize only the L-channel for the FRT data. Multispectral reduced data records (MRDR) comprise 72 channels at 200 m/pixel. The CRISM data are converted to I/F (the ratio of radiance to solar flux measured at the top of the atmosphere), through a series of radiometric, atmospheric and geometric calibrations as described by *Murchie et al.* [2007a, 2007b, 2009a]. This procedure includes a "flat field" correction based on multiple measurements of a bland dusty region in order to correct residual nonuniformities in calibration. MRDR data are delivered to the NASA Planetary Data System (PDS) as a map-projected product and not processed further. However, the standard CRISM FRT I/F data product still contains some column-wise variation, spike and shot noise. A set of standard and accepted correction procedures have been incorporated into the CRISM Analysis Tool (CAT v. 6.3) installed as a plug-in under ITT VIS ENVI 4.5. These include a photometric correction that accommodates nonnormal solar illumination, and an atmospheric correction applied initially to Infrared SpectroMeter (ISM, aboard Phobos 2) [*Bibring et al.*, 1989] and Observatoire pour la Minéralogie, l'Eau, les Glaces, et l'Activité (OMEGA, aboard Mars Express) data [*Mustard et al.*, 2005; *McGuire et al.*, 2009]. It also contains a noise removal and destriping algorithm to address thermal effects, radiation and intrinsic detector measurement error [*Parente*, 2008; *Parente et al.*, 2010]. We apply this standard CAT processing to the data. CAT spectral summary products are calculated for FRT and MRDR images and used for algorithm validation.

[16] The Moon Mineralogy Mapper (M^3) imaging spectrometer aboard the Chandrayaan-1 lunar orbiter was designed to collect data over the spectral interval 430–3000 nm. This instrument also operates in two modes: a full-resolution mode records 261 channels at a nominal spatial resolution of 70 m/pixel, and a global mapping mode that records 85 bands at a nominal spatial resolution of 140 m/pixel. The scene used in this study was acquired with an instrument operating in the mapping mode over the spectral interval 461–2992 nm. Data are delivered to the PDS as radiometrically corrected radiance ($W/m^2\ \mu m\ sr$) with ENVI headers; details are described by *Lundeen et al.* [2010].

2.2. Image Preprocessing

[17] An initial preprocessing performs a light, preliminary pixel-wise cleaning and prepares the spectra for further analysis. We found for CRISM FRT data that some local shot noise persisted after the standard CAT correction procedure. In particular, some thermal switching effects [*Parente et al.*, 2010] remain. A radius 3 median filter in the spectral domain proved an effective remedy; it appeared to improve performance for all subsequent analyses so we incorporated it as a standard preprocessing step that we applied identically to all images in this study. Despite the theoretical possibility of diluting subtle spectral features, the filter is narrower than all of the diagnostic absorption bands we consider, and we found the removal of obvious channelized shot noise and other single-pixel artifacts to be net beneficial for performance of all subsequent analyses.

[18] For each data set, we subset the spectral domain to exclude the noisiest short-wavelength channels as well as strong thermal emission effects; we use the 1002–2602 nm channels for the CRISM data and 750–2737 nm for M^3. In the case of M^3 data, we perform an approximate reflectance computation by normalizing each spectrum to have unit area under the curve; this involves scaling the overall magnitude and dividing the spectrum by the sum of reflectances in all bands. This ensures that all spectrum magnitudes are approximately equivalent across incidental change in illumination due to camera position and surface geometry. We subsequently divide by the mean spectrum of the image to

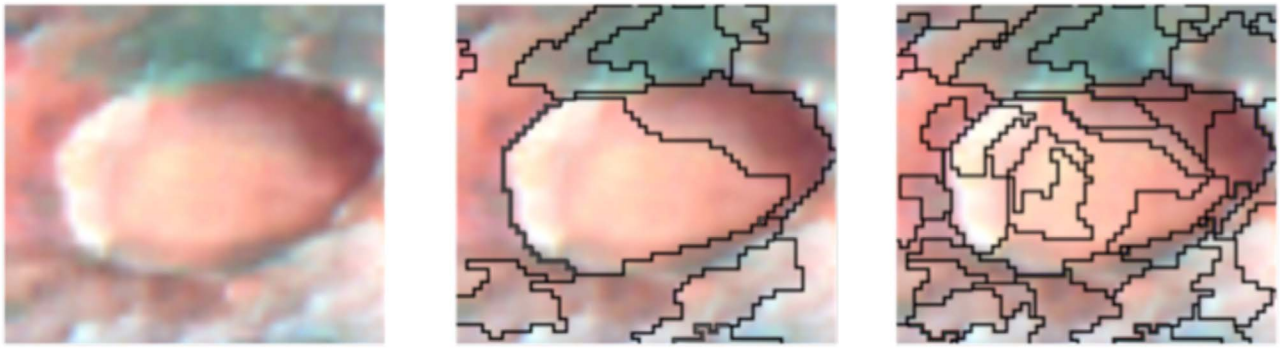

Figure 1. Superpixel segmentation. (left) Original subimage from CRISM FRT00003e12. (middle) Coarse superpixel segmentation. (right) Fine superpixel segmentation.

mask the contribution of the incident spectrum and base substrate. For a nonemissive Lambertian surface, we found that these simple steps mitigated interimage variation and emphasized absorption features. The M^3 preprocessing produces spectra that are not true reflectance values, but are still amenable to end-member detection and subsequent comparison to mineral reflectance spectra in spectral libraries. This is adequate for target detection, but we naturally discourage the use of these spectra for authoritative mineralogical identifications or abundance estimation.

2.3. Superpixel Analysis

[19] Superpixel analysis partitions the image into a set of spectrally homogeneous regions, exploiting our expectation that physical features are spatially contiguous (Figure 1). Ideally, each superpixel corresponds to a single scene feature (e.g., an outcrop, crater, or volcanic flow), and its component pixels are independent reflectance measurements of a single surface material. A superpixel's mean spectrum is a good estimator of this reflectance, and the set of all such superpixel spectra acts as a compact, noise-reduced description of the scene features. Naturally, the best noise reduction would be achieved by superpixels that are as large as possible, such that each physical feature is associated with just one superpixel. Unfortunately this "perfect segmentation" is difficult to achieve in practice (even by hand) and risks diluting or erasing small physical features whenever a single large superpixel overlaps multiple materials. As a compromise, one can still glean noise reduction benefits by erring on the side of oversegmentation such that most or all scene features are associated with multiple superpixels, but no single superpixel crosses the border of a physical feature. The appropriate mean size of the superpixels in a scene is determined by the amount of noise present and the smallest area of contiguous scene features one aims to preserve.

[20] For this work we favor a simple graph-based segmentation algorithm by *Felzenszwalb and Huttenlocher* [2004]. We will review it briefly here and refer the reader to *Thompson et al.* [2010] for a more detailed description of the implementation. We treat the pixels of the image as an 8-connected graph of nodes (Figure 2). A spectral distance metric defined by the user defines a weight on every edge of the graph and permits comparison between neighboring spectra. It also defines a "minimum distance" between neighboring superpixels, given as the smallest distance associated with any edge that bridges the two superpixels. For our work we use a Euclidean distance metric but others are possible such as the Spectral Angle or a more sophisticated user-defined distance score that emphasizes key spectral bands. The algorithm iteratively agglomerates pixels into larger clusters while attempting to maintain the internal spectral homogeneity of each superpixel. A final "region joining" step merges superpixels that are smaller than a predefined minimum region size onto their next spatially closest superpixel. The final output is a membership mapping between individual pixels and the superpixel to which they belong. These superpixels may then have their average spectrum calculated, producing a set of cleaner spectra numbering far less than the original data set (often by two orders of magnitude or more). This final spectral set manifests significantly reduced spectral noise without the diluting effects a simple spatial average would incur while also

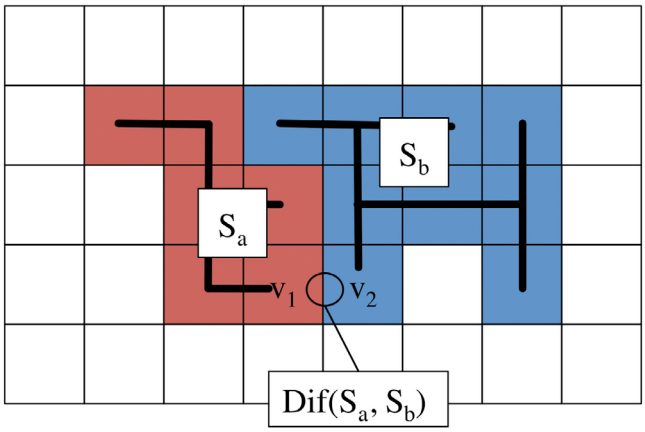

Figure 2. Superpixel segmentation process. The superpixel segmentation algorithm iteratively merges adjacent clusters of spectrally similar pixels (white squares) based on pairwise spectral differences along the border pixels. Here the algorithm considers a merge between segments S_a and S_b. The image pixels v_1 and v_2 are the most similar border pixels. Their difference defines a minimum distance between the two segments $Dif(S_a, S_b)$. The algorithm compares this value to intersegment distances of the minimum spanning tree in each independent segment (illustrated here by thick black line segments) to determine if the two segments can be merged.

reducing computational requirements for later processing due to the smaller number of spectra to further process.

2.4. End-Member Detection

[21] After transformation to superpixel spectra, an automated end-member detection step derives pure constituents based on statistical properties of the data. This stage disregards spatial information, operating on the entire list of independent superpixel spectra from the first stage. Here we presume a simple linear mixing model in which each observed spectrum is a linear combination of the reflectance spectra of the scene end-members. For this model, the Sequential Maximum Angle Convex Cone (SMACC) algorithm [*Gruninger et al.*, 2004] was identified as a top performer in a previous cross-planet and cross-platform study of superpixel end-member detection [*Thompson et al.*, 2010]. The SMACC algorithm functions by maintaining a list of best end-member candidates, and grows it iteratively by adding the spectrum with the largest orthogonal projection onto the subspace spanned by the current set of end-members. This procedure identifies a subset of the spectra that spans the largest possible data volume. A second method called N-FINDR was also evaluated; it represents the class of end-member detection algorithms that indentify all end-members simultaneously. In these tests, SMACC offered comparable performance as well as a significant speed advantage over N-FINDR, so we will use it exclusively here.

[22] The result of the end-member detection operation is a list of n end-member spectra, where the user defines n at runtime. In addition to the mean spectra, the algorithm can supply the superpixel regions associated with each end-member (e.g., as regions of interest in ENVI) so that the user can trace the mineralogical signatures back to specific regions in the scene. By permitting the algorithm to detect more end-members, the user receives a more complete description of the data that is more likely to include subtle mineralogical signatures. The cost of this additional sensitivity is additional human analysis time for the larger candidate spectra list and redundant end-members that are only subtly different. We anticipate users with CRISM-like images will commonly request between 5 to 20 end-members depending on the inherent complexity of the scene, the subtlety of the anticipated features, and the time available to analyze the results.

[23] In our experience, the basic procedure generalizes without difficulty to a range of instruments and scenes. The two user-defined parameters, the size of the superpixels to extract, and the number of end-members to return, are stable across data sets. Previous experiments used identical parameter settings for hyperspectral images as diverse as Airborne Visible/Infrared Imaging Spectrometer (AVIRIS) Cuprite, NV data and the Galileo NIMS data; these trials demonstrated consistent performance across data sets [*Thompson et al.*, 2010; *Bunte et al.*, 2011]. For SMACC-based end-member extraction, the scene was usually best described by the top 10–20 end-members and a minimum superpixel size of 50 image pixels. Naturally, *radically* different spatial resolutions may still require changes; in the multispectral data sets referenced later a minimum superpixel size of 10 is used to accommodate the fact that the anticipated scene features are much smaller with respect to individual pixels.

[24] These end-member spectra may be scientifically interesting in themselves, but here we are concerned with their utility as a "focus of attention" tool to identify and localize novel mineralogy. One natural method to evaluate this is by generating spectral angle intensity maps by projecting all image superpixels onto each end-member spectrum. This yields a new image of n channels, which are then assigned to a mineralogical class by the user. Both end-member maps and CRISM summary products localize key mineral signatures in the image, but using distinctly different approaches. The CRISM summary products leverage hand-tuned spectral features designed for specific mineralogical slope and absorption features, while the superpixel end-member detection method operates in a mostly data-driven, unsupervised fashion. It relies only on statistical properties of the data and a few weak assumptions about how they are generated (spatial continuity, linear mixing). We hypothesize that the combination of superpixel averaging to reduce scene-specific noise and our data-driven classification approach can provide additional utility for these analyses by finding spectral features that were not anticipated beforehand.

2.5. Evaluation as a Focus of Attention Cue

[25] We performed experiments aimed to quantify both the intrinsic value of superpixel end-member detection as a focus of attention tool in and of itself and vis a vis the CRISM summary products in common use. Any such comparison is limited by the fact that no ground truth mineralogy is available for the CRISM data set. Rather than recover "true" mineralogy, we will quantify the ability of each method to discriminate between the key distinctions identified by a trained geologist's thorough manual study. We begin by selecting a series of images from current studies and the CRISM literature whose mineralogy is well characterized [*Bishop et al.*, 2008a; *Milliken et al.*, 2008; *Ehlmann et al.*, 2009, 2010; *Murchie et al.*, 2009b; *Lichtenberg et al.*, 2010]. We manually label most pixels in the image as members of distinct mineralogical classes by identifying spectral end-members and applying a Spectral Angle Mapper (SAM) classification [*Kruse et al.*, 1993] that is adjusted empirically. These are not absolute mineralogical classifications; instead, they indicate general mineral categories and best guess estimates at the principal distinctions in surface material. Not all pixels in the image are classified; those with highly mixed or ambiguous mineralogy may be left unlabeled. The end result is a manual mineralogical classification that defines a "ground truth" by which to judge the focus of attention tools' power to distinguish materials of interest.

[26] Formally, for an image with m manually defined mineral classes we define m different detection problems, each of which can be treated as a separate binary classification task with the goal of recovering a specific mineral type. In other words, a focus of attention image should correlate with manual classifications such that one could threshold the map at some value and recover the manual classification. The best threshold is unknown, so our approach measures the true positive and false positive detection rates for every possible threshold. This receiver operating characteristic (ROC) curve [e.g., *Fawcett*, 2006] quantifies the discriminative power of a single end-member to find a single target material.

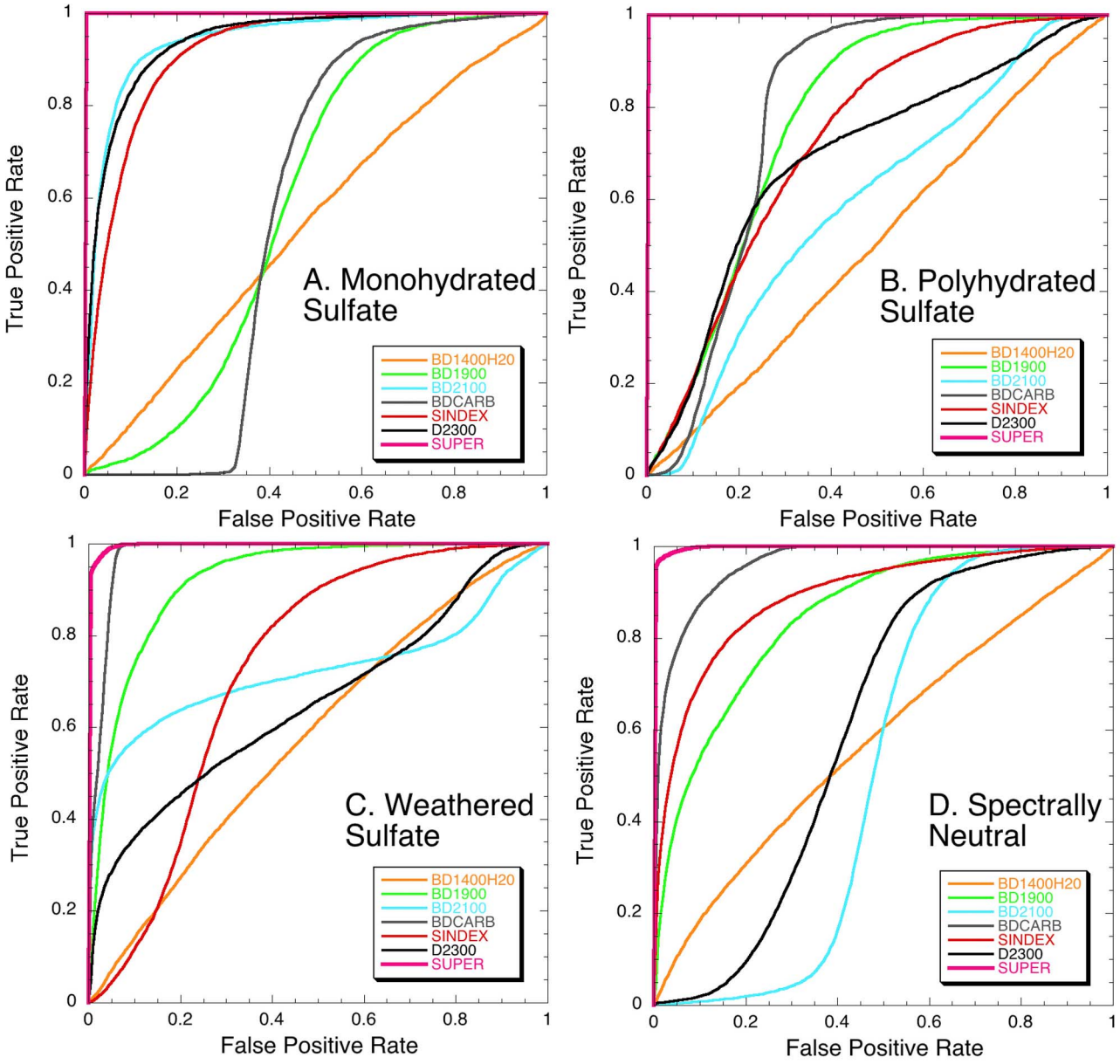

Figure 3. Receiver operating characteristic (ROC) curves evaluating the performance of the superpixel (SUPER) method and six CRISM summary products to classify the four target materials identified manually in image FRT000098b2. A perfect classification (all true positives and no false positives) plots on the top left portion of Figures 3a–3d; a random (poor) classification plots as a line with slope of 0.5 (true positives = false positives).

[27] Example ROC curves are shown in Figure 3. The horizontal axis gives the false positive rate: the fraction of nonmineral pixels that are detected for a particular threshold. The vertical axis shows the true positive rate, defined as the fraction of real mineral pixels that are detected. A naïve detection strategy that chooses pixels at random would show no preference for mineral or nonmineral pixels and would detect each in proportion to its abundance in the scene. Therefore it would have theoretical performance equal to a diagonal line and a 0.5 area under the ROC curve. More discriminative approaches move the curve to the upper left, in which few false positives are required to detect the majority of true positives. For subtle target features subtending a small fraction of the scene, the most important regime is the extreme left of the curve representing thresholds that select only a small portion of image pixels. This represents a situation where the analyst has used a strict threshold to find isolated or rare mineralogy.

[28] The total area under the ROC curve (AUC) is often used as a proxy for average classification performance when comparing two classifiers. The AUC represents the probability that a randomly chosen true positive instance will have a higher classification performance score than a randomly chosen true negative instance [*Fawcett*, 2006]. The AUC is

Table 1. CRISM Summary Products Used in ROC AUC Analysis[a]

CRISM Scene FRT0000xxxx	Spectral Class	Source[b]	Highest-Ranking Acceptable CRISM Index
3e12	Olivine	1, 2, 3	OLINDEX, sensitive to olivine
	Fe/Mg Smectite	2, 3	D2300, depth of 2300 nm absorption
	Magnesite	3	BDCARB, sensitive to carbonate
	Neutral		BDI2000, depth of 2000 nm absorption
3fb9	Phyllosilicate		D2300
	Carbonate	4	BDCARB
	Olivine		OLINDEX
	Neutral		BDI2000
863e	Nontronite		D2300
	Kaolinite	5	BD2210, depth of 2210 nm absorption
	Fe/Mg Smectite	5	D2300
	Montmorillonite	5	BD1900, depth of 1900 nm absorption
	Neutral		BDI2000
abcb	Kaolinite	3, 6	BD2210
	Serpentine	3, 6	D2300
	Olivine	6	OLINDEX
	Neutral		BDI2000
7d87	Gypsum		BD1900
	Sulfate	7	SINDEX, sensitive to sulfates
	Kaolinite	7	BD2210
	Neutral		BDI2000
5814	Sulfate	8	SINDEX
	SiOH	8	BD1900
	Neutral 1		VAR, sensitive to olivine and pyroxene
	Neutral 2		BD1000IR, depth of 1000 nm absorption
	Neutral 3		ISLOPE1, sensitive to ferric coatings on dark rocks
98b2	Monohydrated sulfate	9	BD2100, depth of 2100 nm absorption
	Ferric Hydroxysulfate	9	BD1900
	Polyhydrated Sulfate		BD1900
	Neutral		BDI2000
64d9	Fe/Mg Smectite	2, 3	D2300
	Phyllosilicate		BD1900
	1 μm-rich dust		OLINDEX
	Low-Ca Pyroxene	2	BDI2000
	Neutral		ISLOPE1

[a]CRISM index names from *Pelkey et al.* [2007] and *Roach et al.* [2009].
[b]Sources are 1, *Mustard et al.* [2008]; 2, *Mustard et al.* [2009]; 3, *Ehlmann et al.* [2009]; 4, *Ehlmann et al.* [2008]; 5, *Bishop et al.* [2008a]; 6, *Ehlmann et al.* [2010]; 7, *Murchie et al.* [2009b]; 8, *Milliken et al.* [2008]; 9, *Lichtenberg et al.* [2010].

computed for end-member spectra selected by the superpixel end-member detection method as well as for relevant CRISM summary products for comparison. For m minerals and n end-members, $n \times m$ such comparisons are possible but it is likely that only one or two end-members (or CRISM summary products) are relevant for each manually defined mineral type. Thus, we will consider only the top-performing end-member and relevant CRISM index for each of the m manual categories, where the area under its ROC curve determines the top performer.

3. Results

3.1. Evaluation of the Method

3.1.1. Performance of Method as Compared to Manual Selection of End-Members in CRISM Full-Resolution Images

[29] We manually identified 35 spectral classes in 8 CRISM FRT images. These classes include spectra that appear to be dominated by a single mineral (e.g., olivine, opaline silica), mineral classes (e.g., sulfates, phyllosilicates), and regions that were relatively spectrally flat or neutral (Table 1). In each run, the minimum superpixel size was set to 50, and 10 end-members were solicited. In every image, the superpixel method successfully identified each class ($n = 4$ or 5) that was identified in the manual labeling (Figures 4 and 5).

[30] The remaining 5 or 6 end-members identified by the algorithm generally consisted of additional examples of the manually identified classes. A typical example is image FRT000098b2 (hereafter "98b2" for this and other CRISM FRTs; Figures 4 and 5). Four classes were identified manually: a monohydrated sulfate, a polyhydrated sulfate, a weathered polyhydrated sulfate and a spectrally neutral class. For two of the classes, the algorithm identified two example end-members that are spectrally similar but that differ in albedo and/or the shape of the noise, particularly in the 1.5–1.8 μm region. Albedo likely also contributed to the algorithm's selection of two shadow end-member spectra (Figure 5d). In image 98b2, the algorithm also identified a spectral end-member that was overlooked in the manual labeling. This class is consistent with a ferric hydroxysulfate identified by *Lichtenberg et al.* [2010] (Figure 5e).

[31] Example ROC curves for the superpixel end-member detection and CRISM index methods are shown in Figure 3 and are typical of the data set. The ROC curves plot in the top left portion of Figures 3a–3d corresponding to a high true positive rate (high sensitivity) and low false positive rate (high specificity). SAM maps of class end-members constructed at low false positive rate thresholds agree well spatially with manual classification (Figure 6).

[32] The average performance of the superpixel segmentation and SMACC end-member detection is evaluated using

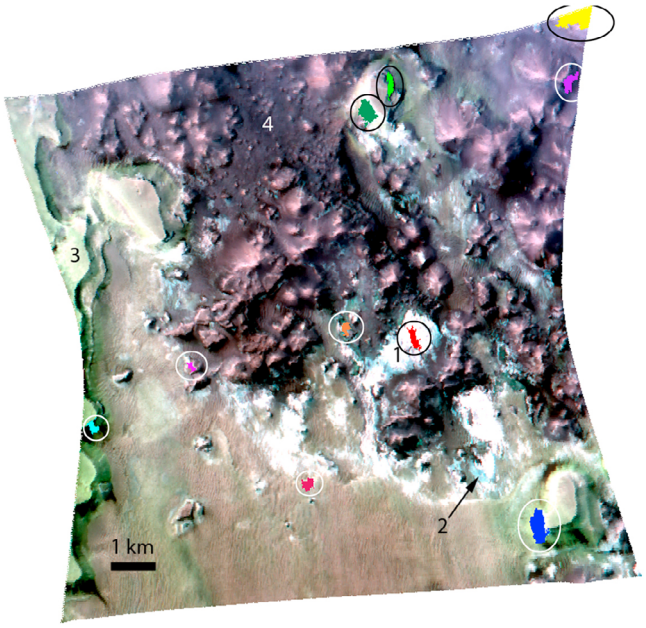

Figure 4. CRISM image FRT000098b2 in Aram Chaos. RGB = 2.51, 1.49, and 1.09 μm. North is up. Four classes are identified manually and are numbered: Class 1 (white tones) is monohydrated sulfates, class 2 (blue tones) is polyhydrated sulfates, class 3 (green tones) is weathered polyhydrated sulfates, and class 4 (purple tones) is spectrally neutral materials. Ten spectral end-members identified by the automated superpixel algorithm are indicated by regions of interest of varying colors (circled) and are keyed to spectra in Figure 5.

area under the ROC curve data (Figure 7). All AUC values lie between 0.5, which is the value of random guess and 1, which is a perfect discrimination of mineral end-members. For example, an AUC value of 0.90 means that 90% of the time, any pixel containing a particular mineral has a classification statistic value for that mineral greater than that of any pixel that does not contain that mineral. Typically AUC values are treated like an academic grading system, where a value ≥90 is considered excellent discrimination, ≥80 good, etc. The AUC values for the superpixel method cluster very close to 1, with a mean value of 0.97 ± 0.07 and a median value of 0.998. The superpixel method superbly discriminates the spectra of target materials.

[33] While the average AUC statistic is excellent, it is useful to examine the mineral classes with the poorest performance. All of the data (n = 5) that score <0.946 belong to one of two images, 64d9 and 5814. In both images, some spectral end-members were difficult to isolate manually because the targets contained mixtures of minerals in varying proportions. In this situation, the hand-labeled end-members meet a conservative (and arbitrary) threshold criterion, where the spectra of member pixels were dominated by a particular mineral, but often contained other minerals. A superpixel containing a mixture of the two minerals will match the "ground truth" best only for the most conservative criteria (lowest false-positive rates), which are likely the pixels with mixtures that best mimic the proportions in the ground truth data.

3.1.2. Performance Compared to CRISM Summary Products

[34] To compare the superpixel end-member detection strategy with the current practice, we also generated ROC statistics for each of the CRISM spectral summary parameters. An acceptable CRISM index was identified for each mineral class (Table 1). Some classes could have more than one acceptable CRISM index, for example, many phyllosilicate minerals have both an absorption near 2300 nm that corresponds to the D2300 CRISM index and an absorption at 1900 nm (BD1900 index, see Table 1 for index explanations). Acceptable CRISM index matches for spectrally neutral end-members in a scene included parameters associated with mafic mineralogy (BDI2000, VAR, OLINDEX, BD1000IR) or ferric dust (ISLOPE1). The ROC curve of the highest-ranking acceptable CRISM index was compared to the superpixel end-member data.

[35] ROC area under the curve statistics show that the CRISM summary products perform significantly better than random in the majority of cases (Figure 7). It is important to note that in 5 of the 11 cases where the CRISM method performs poorly (<0.80), it is classifying end-members labeled as spectrally neutral. The CRISM parameters were designed to detect specific minerals and most spectrally neutral pixels have no obvious or standard mineral assemblage. Thus, for parity, we omit the neutral pixel data from the mean AUC statistic to report a mean AUC value for the CRISM data of 0.87 ± 0.12 and a median value of 0.899.

[36] The superpixel end-member strategy performs better on average than the CRISM summary products for 97% of the cases (n = 34). Examination of the shape of the ROC curves show agreement with the AUC statistic, where in most cases, the superpixel ROC curve lies to the upper left of the CRISM index indicating its higher average accuracy (Figure 3). The ROC curves can also be used to evaluate the performance of the CRISM summary products. Figure 3 shows ROC curves generated for 6 CRISM summary products for each the four classes identified manually. The top three performing CRISM summary products for the monohydrated sulfate are BD2100, D2300, and SINDEX. Examination of the spectrum of this class (Figure 5a) shows absorptions at 2.11 μm and 2.39 μm consistent with the BD2100 and SINDEX [*Pelkey et al.*, 2007; *Roach et al.*, 2009]. The D2300 response may be the result of a spectral slope induced by the sharp 2.39 μm band (Figure 5a). The near-diagonal line performance of BD1400H2O (depth of 1400 nm absorption) on each of the ROC curves shows that this metric has no predictive capability for the materials in this scene. Examination of Figure 3a also shows two summary products that perform worse than random at low false positive rates. These summary products are sensitive to something in this scene, but this information is incorrectly applied.

[37] As determined by the AUC statistic, the three top performing CRISM summary products for both polyhydrated sulfate classes are BDCARB, BD1900, SINDEX, respectively. While the BD1900 and SINDEX summary products are tied to diagnostic mineral absorptions in polyhydrated sulfates and are expected to perform well, the BDCARB index is likely responding to the paired 2.39 and 2.53 mm absorptions in these spectra (Figures 5b and 5c). These absorptions are typical of several polyhydrated sulfates (e.g., melanterite, rozenite) in addition to carbonates; melanterite

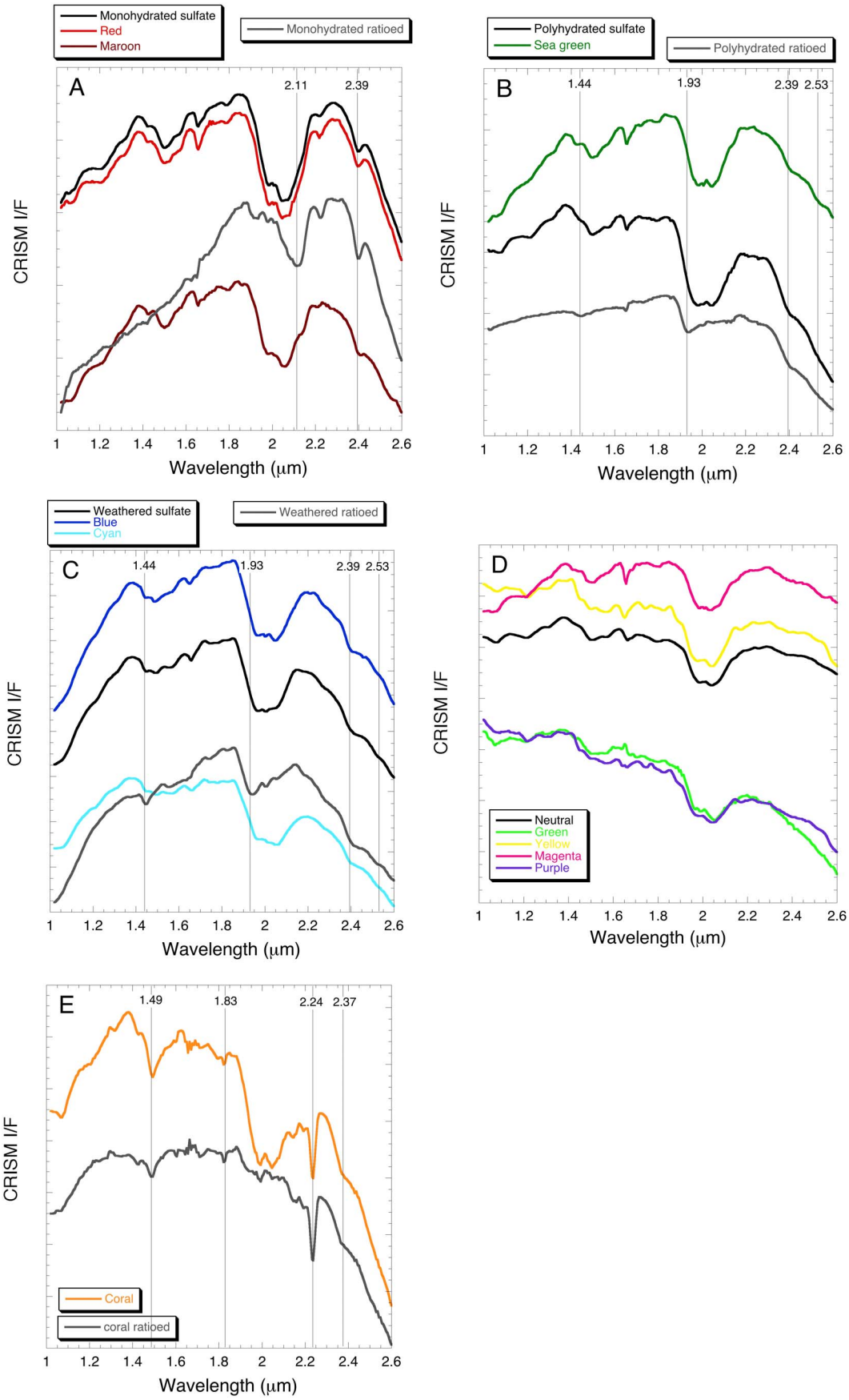
Monohydrated sulfate
Red
Maroon
Monohydrated ratioed
A
2.11
2.39
CRISM I/F
Wavelength (μm)
Polyhydrated sulfate
Sea green
Polyhydrated ratioed
B
1.44
1.93
2.39 2.53
Weathered sulfate
Blue
Cyan
Weathered ratioed
C
D
Neutral
Green
Yellow
Magenta
Purple
E
1.49
1.83
2.24 2.37
Coral
coral ratioed

Figure 5

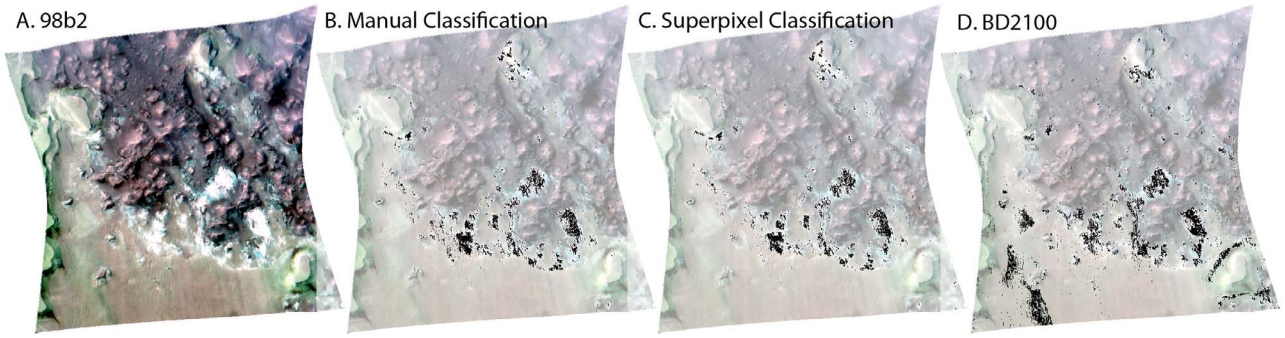

Figure 6. Image classification results (in black) for monohydrated sulfates. (a) CRISM image FRT000098b2; bands as in Figure 4, monohydrated sulfates appear white. (b) Manual classification mapped using Spectral Angle Mapper (SAM). (c) Automated superpixel classification mapped using SAM. (d) Threshold map for CRISM index BD2100, an indicator of monohydrated sulfate.

was suggested as a candidate mineral in this image by *Lichtenberg et al.* [2010]. Although the SINDEX has the 3rd ranked AUC statistic, the ROC curve shows that this index performs poorly under the conservative criterion of low false positives. The SINDEX performs well only at the expense of a large number of false positive detections and is thus not as sensitive indicator of this polyhydrated sulfate class as BDCARB or BD1900.

[38] In general, both the superpixel technique and CRISM summary products appear to work comparably at the highest AUC values (>0.90), and the performance of both methods degrades in concert (Figure 7). Like the superpixel strategy, the CRISM summary products also perform poorly on images 64d9 and 5814, which supports the idea that the spectral end-members in these images were not well represented by the pure mineral targets of the CRISM summary products. This result is consistent with the end-members being mixtures of materials in varying abundances or being spectrally featureless.

3.1.3. Performance in Other Data Sets

[39] One advantage to the superpixel method is its adaptability to a range of hyperspectral data sets. The method has been demonstrated on AVIRIS [*Thompson et al.*, 2010] and NIMS data [*Bunte et al.*, 2011]. Here we describe three proof-of-concept experiments to demonstrate the potential application of this method to new issues.

3.1.3.1. CRISM MRDRS

[40] A primary motivation for the development of the superpixel method was to produce an automated method that could analyze large data sets quickly enough to allow rapid decision making about subsequent observations. A CRISM MRDR scene (t0943_mrrif_05s343_0256_1, hereafter "943") in Iani Chaos was analyzed using the superpixel method, setting the number of requested end-members to 10. Compositional and geomorphic mapping of this region [*Gilmore et al.*, 2010] identified several sulfate deposits lying among units that are spectrally flat in the 1.0–2.6 μm region (Figure 8a, in pink). Three of the 10 end-members comprise sulfate; the remaining end-members included several examples of the spectrally neutral materials, shadow and bright materials. Three sulfate end-members were identified using the superpixel method and a mineral map produced using the SAM algorithm (Figure 8b). Note the good spatial correspondence of the automatically derived end-members (Figure 8b) to the sulfates mapped manually (Figure 8a). The automated end-members also compare well spatially to results of the SINDEX (Figure 8c). Comparison of the superpixel method and the SINDEX (single pixel method) shows some potential advantages of the former. As expected, the superpixel averaging and the preprocessing filtering result in a less noisy image prior to classification. These noise reduction steps may amply true signals that could be lost in per pixel classification scheme (e.g., the site indicated by the arrow in Figure 8b versus Figure 8c). Because the superpixels are clustering pixels of like spectral character, the resulting classification identifies spatially contiguous regions that are more likely to represent real geologic phenomena. For example, the sea green unit in Figure 8b is a reasonable match for sulfates, but also a match for another spectral unit on the mesa tops that warrants further investigation.

3.1.3.2. Chandraraayan-1 M^3 Data

[41] An M^3 image for a region on the lunar nearside was analyzed to estimate the utility of this method for this newly released data. Twenty end-members were solicited for this spatially large image (~4.2×10^6 pixels), with a minimum superpixel size of 20. Ten of the end-members exhibit two absorptions at ~1000 and 2000 nm consistent with the mineral pyroxene (Figure 9, spectra 1, 4, 6, 8, 11, 12, 14, 16, 18). High-Ca clinopyroxenes, with absorptions ~980 and ~2100 nm (e.g., spectra 1 and 12), can be distinguished from low-Ca clinopyroxenes or orthopyroxenes with absorptions ~940 nm and ~1900 nm (e.g., spectra 6, 8, 18 [e.g., *Adams*,

Figure 5. Averaged spectra of spectral classes indentified manually (black) and spectral end-members detected automatically (colors) in image FRT000098b2. The colors of the end-member spectra are keyed to the same hued regions of interest (ROIs) in Figure 4. (a) Monohydrated sulfate class, (b) polyhydrated sulfate class, (c) weathered polyhydrated sulfate class, and (d) spectrally neutral class, including the shadow end-member class (green and purple spectra). (e) The "coral" end-member class was detected only by the automated method and is consistent with ferric hydroxysulfate identified by *Lichtenberg et al.* [2010]. Ratioed spectra in each image are black (or colored) spectrum/yellow spectrum of Figure 5d.

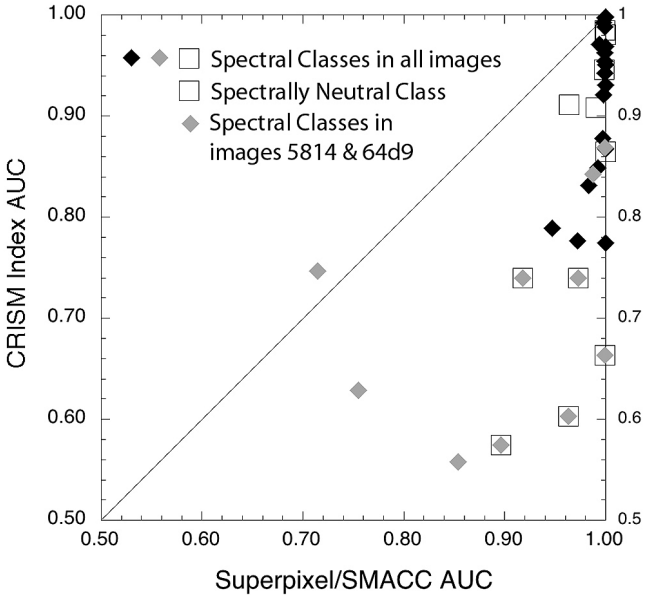

Figure 7. Area under the ROC curve (AUC) statistic for each spectral class (e.g., mineral x in image y) classified by both the superpixel SMACC method and CRISM CAT summary products method (see Table 1). A value of 1 is a perfect classification. Open squares represent pixels classified manually as spectrally neutral; CRISM summary products are not optimized for their detection. Note overall poor performance of both classifiers for images FRT00005814 and FRT000064d9 (gray diamonds).

1974]). Olivine spectrally dominates end-members 5 and 17, recognized by a broad absorption ~1050 nm [e.g., *Hunt and Salisbury*, 1970]. Plagioclase-rich materials lack prominent absorptions [e.g., *Hunt and Salisbury*, 1970] and thus may or may not be represented by several of the linear spectra (e.g., 15, 19), some of which show an increasing reflectance toward longer wavelengths in noncontinuum removed spectra as has been documented for lunar highland rock powders and soils [*Pieters*, 1993].

[42] All of the automated end-members (n = 16) that were not noise are located within craters or, in one case, a graben (Figure 10). Noisy spectra were identified by the user and typically included sharp discontinuities. Lunar craters expose fresh materials from beneath weathered regolith. This is seen in Figures 10a and 10b where olivine-rich materials exposed

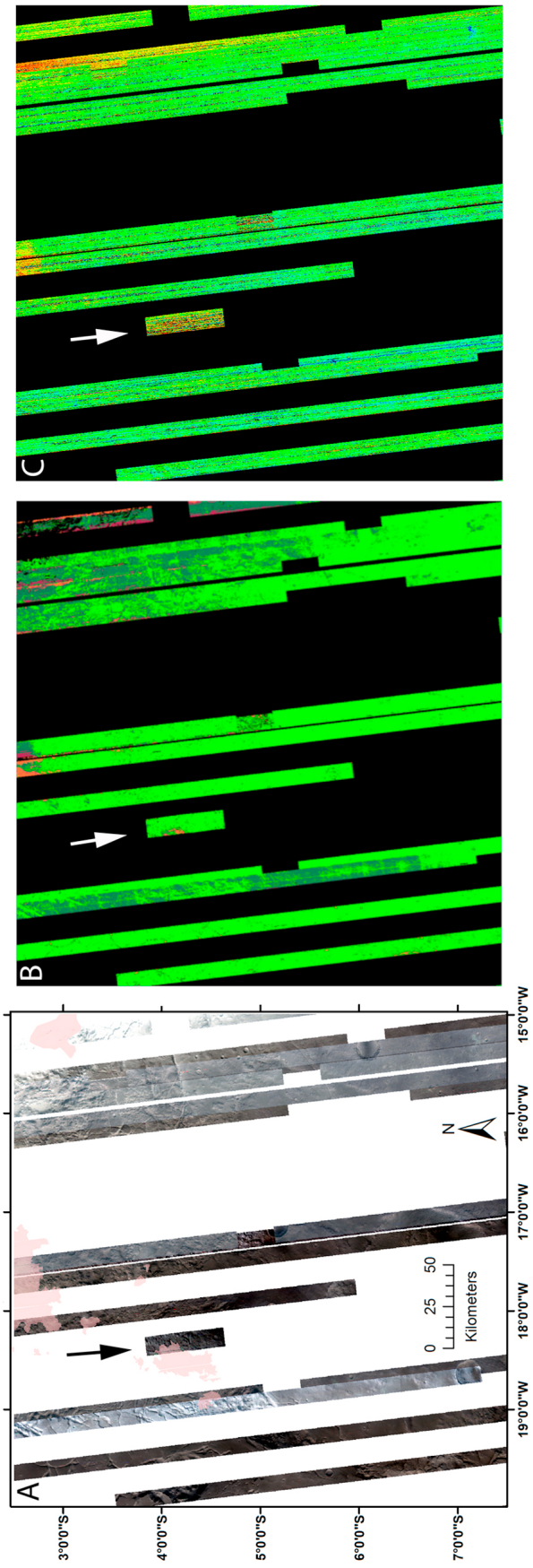

Figure 8. (a) CRISM MRDR image 943 of Iani Chaos, RGB = 2.46, 1.50, and 1.15 μm. Manually mapped sulfate deposits are overlaid in pink. (b) SAM classification of sulfate end-members identified by semiautomated superpixel and end-member extraction methodology. Pink, coral, and sea green hues correspond to sulfates; bright green corresponds to pixels that are classified as nonsulfate materials or unclassified. (c) SINDEX classification of scene, where blues are low values and reds are high values. Note the good spatial agreement between the SAM result and mapped sulfate deposits. Arrow indicates region where the superpixel strategy reduces noise and results in a more spatially realistic classification.

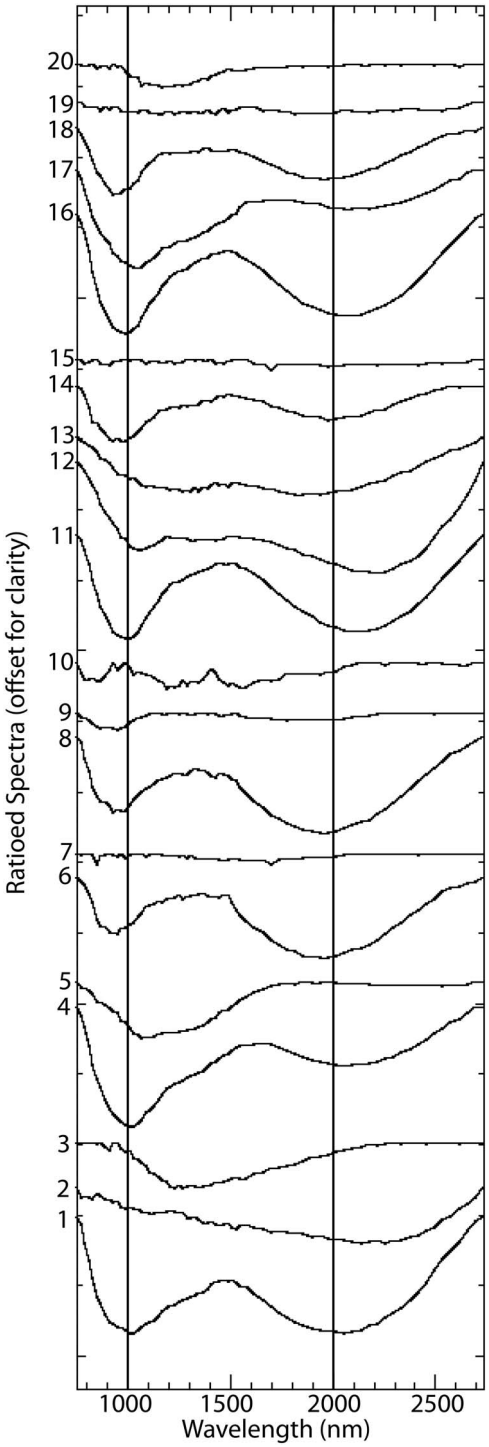

Figure 9. Automated spectral end-members generated for M^3 image M3G20081119T021733; spectra are continuum removed. Vertical lines at 1000 and 2000 nm are for reference. Olivine-rich (e.g., 5, 17) and pyroxene-rich (e.g., 1, 8, 11) materials are included, as well as noise (e.g., 10).

in a crater wall have a stronger spectral signature that the olivine-rich materials in the adjacent regolith. Craters may also excavate materials from depth that contain minerals not plentiful on the surface. This may be the case in Figures 10c and 10d where the largest crater in the scene (deepest excavator) is associated with pyroxene-rich materials. In a single case, a spectral end-member is detected in a graben wall (Figures 10e and 10f). With a single absorption at ~1190 nm, this end-member is unique among the 20, and its spatial

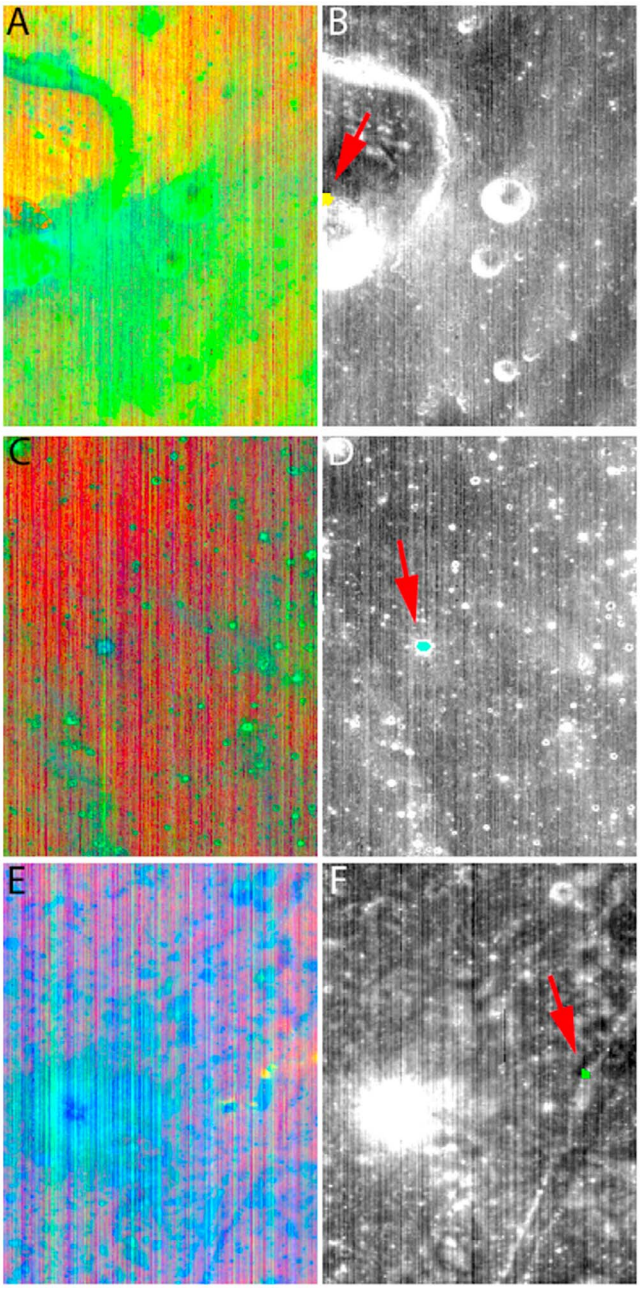

Figure 10. M^3 images of selected superpixel/SMACC end-members. (left) RGB = 2178, 1529, and 1010 nm; olivine–rich materials appear red to yellow and pyroxene-rich materials appear blue to green in this rendition. (right) The 750 nm band with spectral end-member ROI indicated in color (arrows). End-members recognize spectrally distinct materials exposed on (a–d) crater and (e and f) graben walls. In Figure 10b, spectrum of ROI is 5 in Figure 9; in Figure 10d, spectrum of ROI is 6 in Figure 9; and in Figure 10f, spectrum of ROI is 20 in Figure 9. Images are ~30 km across.

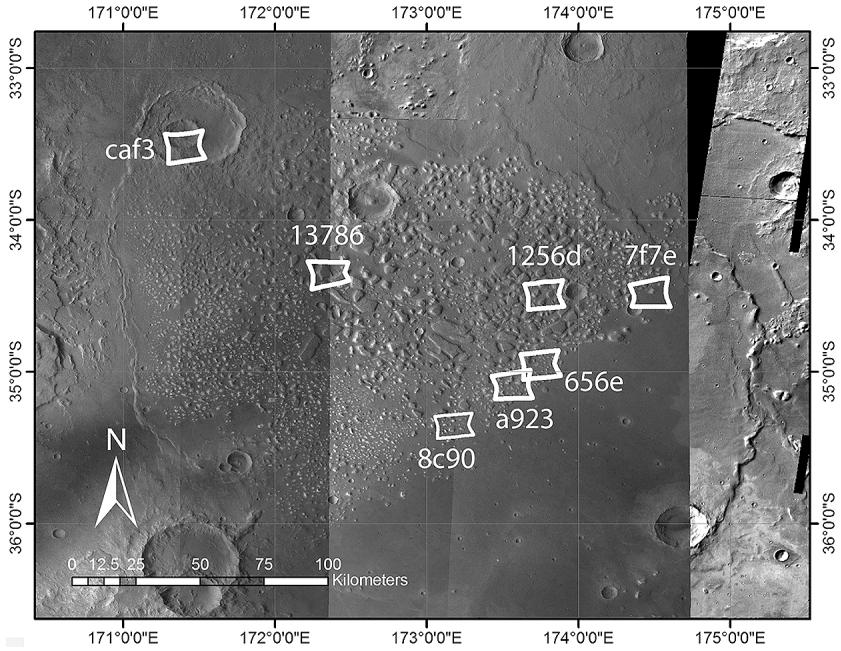

Figure 11. Image mosaic of Ariadnes Chaos. Base image is a THEMIS IR daytime 256 pixels/degree mosaic, overlain by HRSC images h4209_000_nd3, h4187_0000_nd3, and h4187_0000_nd4. CRISM footprints of FRT images used in this study are shown and labeled FRT0000xxxx.

association with what may be a volcanic vent (Figure 10f) invites further investigation. In each of these examples, the superpixel-augmented SMACC algorithm recognizes these materials as spectral outliers because they are spectrally distinct from the bulk of the image. This tool is thus well tuned for focus of attention and novelty detection tasks.

3.2. Case Study: Application to Ariadnes Chaos

3.2.1. Introduction and Methods

[43] Here we apply the superpixel/SMACC method to a set of unstudied CRISM images to further evaluate its practical and scientific utility as an analysis tool. We examine seven CRISM FRT images in Ariadnes Chaos (Figure 11). Ariadnes is one of several regions of chaos in Terra Sirenum and has been interpreted to have once been part of a larger Late Noachian/Early Hesperian paleolake system that was the source region for Ma'adim Vallis [*Irwin et al.*, 2004]. Examination of image data shows the floor of Ariadnes to include relatively light-toned mounds, covered by a darker deposit that lies between and on top of the mounds [*Irwin et al.*, 2004] (Figure 11). Bright materials have been recognized in other chaos regions on Mars and found to comprise sulfates and Fe-oxide minerals, consistent with evaporation [e.g., *Glotch and Rogers*, 2007; *Noe Dobrea et al.*, 2008; *Lichtenberg et al.*, 2010]. The mineralogy of bright materials here may yield insight into the composition and duration of waters that once occupied Ariadnes basin.

[44] The CRISM images were analyzed using Hii-HAT software (http://hyperspectral.jpl.nasa.gov), which incorporates the superpixel/SMACC algorithm. Our workflow for using the automated superpixel segmentation and end-member detection technique includes (1) preprocessing, (2) superpixel segmentation, (3) end-member extraction, (4) examination of the shape and location of individual spectra, (5) ratioing of target spectra to spectrally neutral spectra in the same instrument column to facilitate identification, and (6) production of classification maps of target end-members to characterize class spatial distribution. The classification maps are generated automatically in Hii-HAT for each end-member using the Spectral Angle Mapper [*Kruse et al.*, 1993].

3.2.2. Results

[45] Ten end-members were requested for each image, per our experience with other CRISM FRT data. This resulted in 70 end-members which were found to fall into one of 7 categories: (1) Fe/Mg smectites, (2) Al-smectite, (3) sulfate, (4) olivine, (5) spectra with a 2 μm absorption, likely pyroxene, (6) spectrally flat, and (7) shadow.

3.2.2.1. Smectites

[46] Smectites are 2:1 phyllosilicate minerals typified by absorptions at ~1.9 μm due to H_2O and ~2.3 μm due to cations in the octahedral site, often accompanied by absorptions at ~1.4 μm due to OH and ~2.4 μm [e.g., *Clark et al.*, 1990; *Bishop et al.*, 2008b]. The specific absorptions vary as a function of composition. Nontronite (ideally $Na_{0.3}Fe_2^{3+}(Si, Al)_4O_{10}(OH)_2 \bullet nH_2O$), the Fe end-member, has a band centers near 1.43 μm and 2.29 μm, while the Mg-rich end-members hectorite (ideally $Na_{0.3}(Mg, Li)_3Si_4O_{10}(OH)_2$) and saponite (ideally $(Ca/2, Na)_{0.3}(Mg, Fe^{2+})_3(Si, Al)_4O_{10}(OH_2) \bullet 4(H_2O)$) typically have absorptions at 1.38–1.39 μm and 2.31–2.32 μm; Al-rich smectites typically display absorptions at 1.41 μm and 2.21 μm [*Clark et al.*, 1990; *Bishop et al.*, 2002a, 2002b].

[47] A number of spectra in Ariadnes have strong absorptions at 1.91–1.92 μm and 2.30 μm consistent with a smectite containing both Fe and Mg (Figure 12). Weaker absorptions at 1.41 and ~2.4 μm are common, but not ubiquitous, and also consistent with smectite. While the 1.9 μm absorption is often

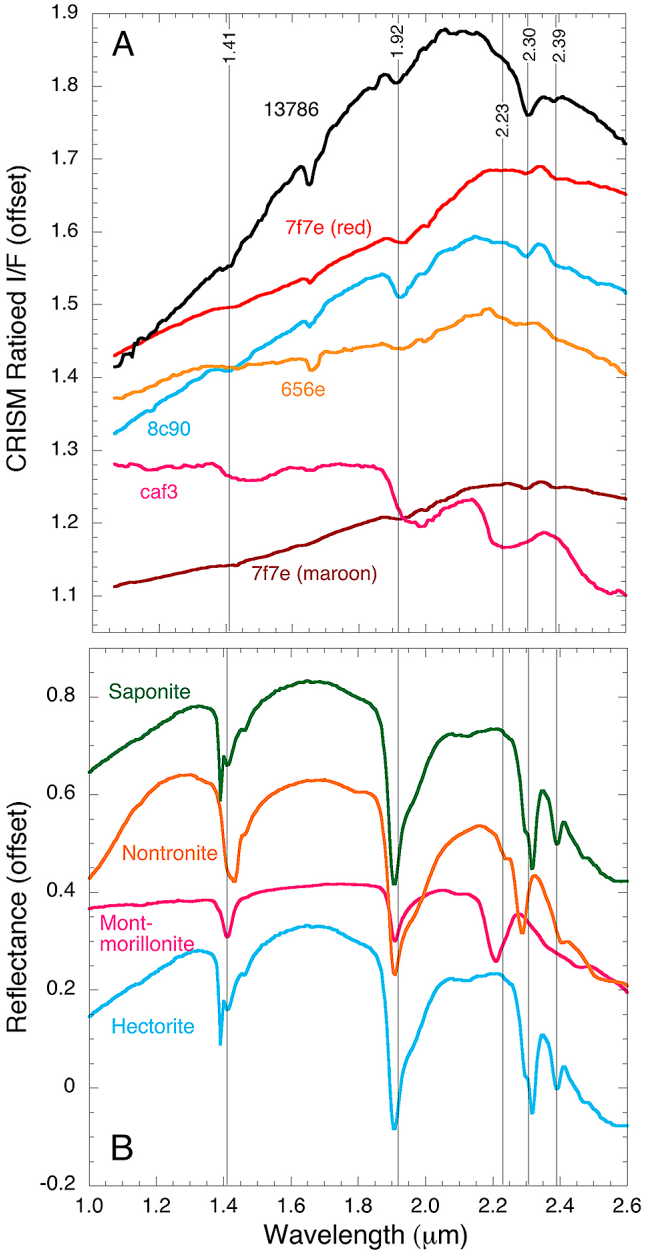

Figure 12. (a) CRISM spectra of smectite-bearing materials in Ariadnes Chaos. Spectra are averages of individual end-member regions selected by the superpixel/SMACC algorithm ratioed by a spectrally neutral region of similar size. Image labels refer to FRT0000xxxx. Major spectral absorptions are indicated by vertical lines. (b) Spectra of smectites from the CRISM spectral library: saponite is sample LASA52, nontronite is CBJB26, montmorillonite is 397F013, and hectorite is BKR1JB172. End-members 7f7e (red) and (maroon) are keyed to colors in Figure 15.

prominent, several spectra identified by the algorithm display a weak 1.9 μm absorption and an absent 1.4 μm absorption (Figure 12, samples from 7f7e and 656e). The strength of these absorptions indicate that these materials have lower water contents, also, weak bands such as the 1.4 μm band may be readily obscured by mixing with other materials (e.g., ferric dust [*Ehlmann et al.*, 2009]).

[48] In image caf3, an end-member is identified with prominent absorptions at ~1.4, ~1.9, and 2.23 μm (Figure 12). These characteristics are consistent with montmorillonite (ideally $(Na, Ca)_{0.3}(Al, Mg)_2Si_4O_{10}(OH)_2 \cdot n(H_2O)$). The absorption features are broader than those seen in laboratory spectra; this effect has been noted in other CRISM spectra and attributed to mineral mixing [e.g., *McKeown et al.*, 2009].

3.2.2.2. Sulfates

[49] In the 1.0–2.6 μm region, OH- or H_2O-bearing sulfates are typified by absorptions at 1.4 μm due to OH, 1.9 μm due to H_2O, and a number of absorptions over the 2.1–2.6 μm region attributed to OH or H_2O combinations or overtones and/or S-O bending or stretching overtones [*Hunt et al.*, 1971; *Bishop and Murad*, 2005; *Cloutis et al.*, 2006]. The algorithm identified several end-members with absorptions at 1.93, 2.40, and 2.53 μm, indicative of sulfates (Figure 13). One class of sulfate end-members (Figure 13, 7f7e spectra) also contains a prominent 2.30 μm absorption that is broader than seen in the smectite end-members. We attribute the strong 2.3 μm absorption in these spectra to smectite and propose that these materials are a mixture of sulfate and smectite. Another type of sulfate end-member (Figure 13, spectra of 12786 and 8c90) displays a strong 1.41 μm absorption, a broad 1.9 μm band, and a steep 2.4 μm band, typical of a range of Fe, Mg, and Ca polyhydrated sulfates.

3.2.2.3. Mafics

[50] In two images, the superpixel/SMACC algorithm selected an end-member with a deep, broad absorption centered on ~1 μm (Figure 14). We identify this as olivine (ideally $(Fe, Mg)_2SiO_4$). Two images also contain an end-member that is dominated by a broad absorption at ~1.98 μm. This is consistent with low-Ca pyroxene, but should be verified with additional examination at shorter wavelengths.

3.2.3. Spectral Stratigraphy and Discussion

[51] The end-members identified by the superpixel/SMACC algorithm were used to generate a classification map for a given image, allowing an assessment of the geographic distribution of end-members. We present a typical example of Ariadnes Chaos morphological and spectral stratigraphy in Figure 15. The sulfates and smectites are limited to the mesas and mounds that lie on the floor of Ariadnes Chaos (Figure 15a). MRO's Context Camera (CTX, 6 m/pixel) and (High Resolution Imaging Science Experiment (HiRISE, ~30 cm/pixel) images show that these materials have a high albedo and are pervasively fractured on the tens of meters scale; this bright and fractured morphology has been noted for other deposits of sulfates and phyllosilicates at many locations on Mars and attributed to desiccation [e.g., *Bishop et al.*, 2008a; *Murchie et al.*, 2009b; *Wray et al.*, 2011]. The fractures often contain fill with a range of albedos; occasionally this fill is exposed by differential erosion and stands higher than surrounding bright material. The bright materials of the mesas are in contact with dark materials that occupy the floor of Ariadnes surrounding the mesas. The dark materials are seen to onlap onto the edges of the mesas or may cover the mesas entirely (Figure 15a). Thus the general history of the region includes (1) the formation of the bright materials, (2) their isolation into mesas and mounds, (3) the emplacement of dark materials around and over the mounds, and (4) erosion to expose bright materials in some of the mounds.

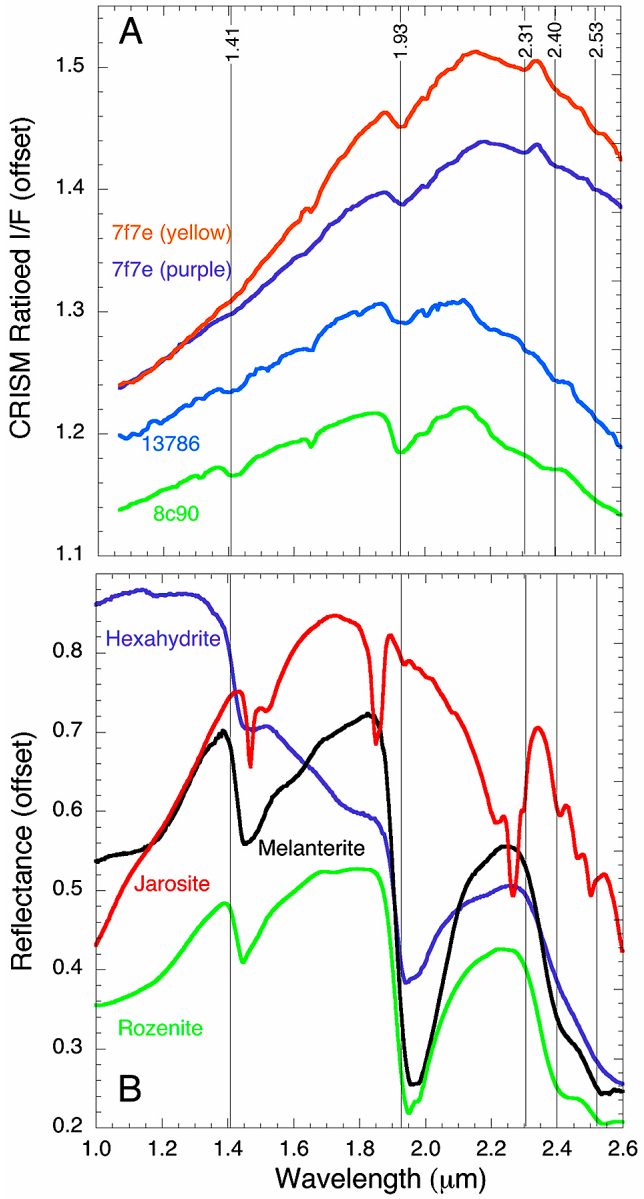

Figure 13. (a) CRISM spectra if sulfate/smectite mixtures in Ariadnes Chaos. Spectra are averages of individual end-member regions selected by the superpixel/SMACC algorithm ratioed by a spectrally neutral region of similar size. Image labels refer to FRT0000xxxx. Major spectral absorptions are indicated by vertical lines. (b) Spectra of sulfates from the CRISM spectral library: hexahydrite (ideally $MgSO_4 \cdot 6H_2O$) is sample LASF56A, melanterite (ideally $Fe^{2+}SO_4 \cdot 7H_2O$) is LASF44A, jarosite (ideally $(Na, K, H_3O)Fe_3(SO_4)_2(OH)_6$) is F1CC11B, and rozenite (ideally $Fe^{2+}SO_4 \cdot 4H_2O$) is BKR1JB626B. End-members 7f7e (purple) and (yellow) are keyed to colors in Figure 15.

[52] The mineralogy recognized here displays a consistent stratigraphy in Ariadnes Chaos, an example of which is shown in Figure 15b. Where bright materials are exposed, the chaos mounds have centers dominated by the sulfate/smectite and smectite end-members. The less hydrated smectites and sulfate/smectites (e.g., the maroon end-member in Figures 15 and 12) are often seen at mound edges, in contact with the dark materials, where the less hydrated materials may follow the contour of the contact with dark material. The spatial relationship between the less hydrated smectites and the dark materials suggests a genetic relationship and we propose that the emplacement of the dark materials facilitated dehydration of underlying smectites. Although the dark materials are spectrally flat, their centimeter to meter scale texture is consistent with volcanic materials. Volcanic materials may have

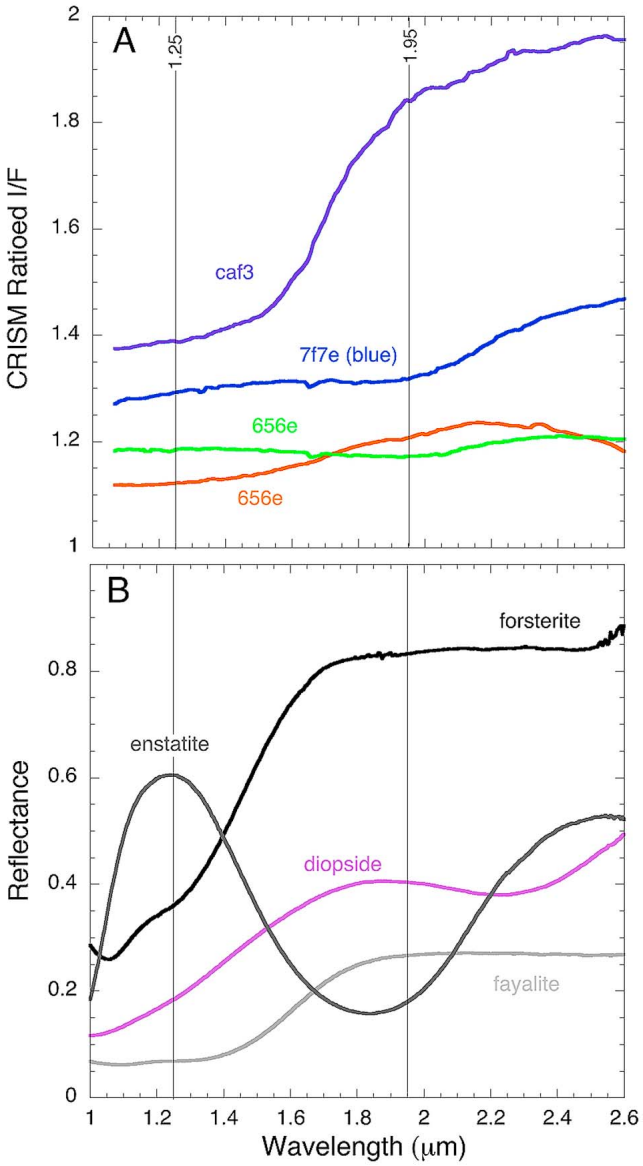

Figure 14. (a) CRISM spectra of mafic materials in Ariadnes Chaos. Spectra are averages of individual end-member regions selected by the superpixel/SMACC algorithm ratioed by a spectrally neutral region of similar size. Image labels refer to FRT0000xxxx. Major spectral absorptions are indicated by vertical lines. (b) Spectra of mafic minerals from the CRISM spectral library: forsterite (ideally Mg_2SiO_4) is sample C3PO51, enstatite (ideally $Mg_2Si_2O_6$) is C5PE32, diopside (ideally $CaMgSi_2O_6$) is C1PP61, and fayalite (ideally Fe_2SiO_4) is C3PO59. End-member 7f7e (blue) is keyed to colors in Figure 15.

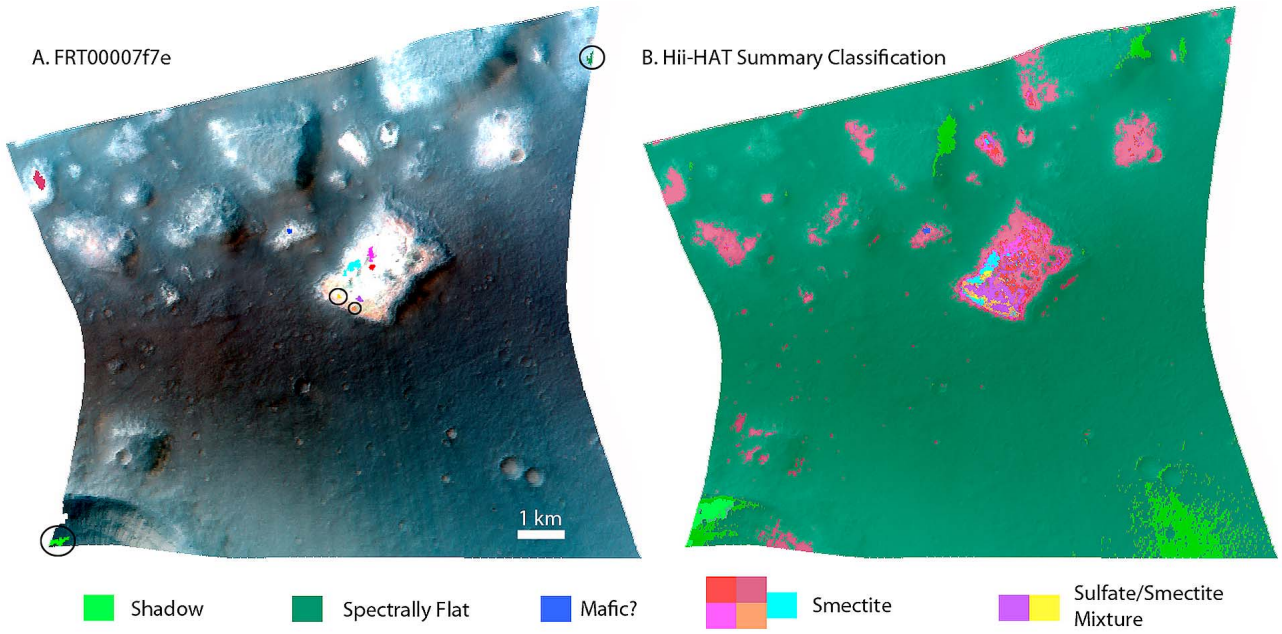

Figure 15. (a) CRISM image FRT00007f7e in Ariadnes Chaos. RGB = 2.51, 1.49, and 1.09 μm. North is up. Ten spectral end-members identified by the automated superpixel algorithm are indicated by regions of interest of varying colors and are circled where emphasis is required. (b) Summary classification of the scene using Hii-HAT software. All pixels are grouped into one of the 10 end-member classes using the Spectral Angle Mapper algorithm. Light-toned areas within the mesas are dominated by smectite and smectite/sulfate mixtures.

heated underlying deposits and facilitated their dehydration. Alternatively, the bright materials may be undergone desiccation at the surface prior to the emplacement of the dark unit.

[53] The sulfate mixtures and smectites are spatially intermingled within the mounds. Analysis of CTX or HiRISE images within the regions covered by the seven CRISM images shows no obvious morphological or textural boundary between the materials. There is also no obvious stratigraphic relationship between the units. This, and the mixed nature of the sulfate end-member spectra, suggests that the sulfates and phyllosilicates are not confined to individual layers, but are mixed at the CRISM scale (~18 m/pixel). While both phyllosilicates and sulfates are indicators of aqueous activity, they are produced in two different environments. Fe/Mg smectites are a common production of weathering and require persistent water-rock interaction in a mildly acidic to alkaline environment [e.g., *Velde*, 1995; *Chevrier et al.*, 2007]. Sulfates are formed by the evaporation of fluids. Thus the juxtaposition of smectites and sulfates constrains their formation mechanism. One model posits the formation of smectites under high water:rock conditions followed at a later time by the precipitation of sulfates, perhaps by the evaporation and S-rich waters or the circulation of S-rich groundwater through the smectite deposit. Another model is that the smectites and sulfates precipitated simultaneously under rapidly changing environmental conditions. This situation is seen in some acid saline lakes in Australia [e.g., *Baldridge et al.*, 2009]. Deposits containing both sulfate and phyllosilicates have been to date observed rarely on Mars, and include Mawrth Vallis [*Farrand et al.*, 2009], Columbus Crater [*Wray et al.*, 2011], Cross Crater [*Swayze et al.*, 2008], Terra Meridiani [*Wiseman et al.* 2008; *Wray et al.*, 2009] and Gale Crater [e.g., *Milliken et al.*, 2010]. The type, location and admixture of sulfates and phyllosilicates in Cross Crater and Columbus crater are interpreted to result from precipitation in paleolakes with limited groundwater inflow, where water levels are controlled by evaporation [*Swayze et al.*, 2008; *Murchie et al.*, 2009b; *Wray et al.*, 2011]. This may also be the case for Ariadnes, where the light-toned deposits are limited to the lowest levels of the basin, below the level required to incise Ma'adim Vallis (the region's primary outflow) [*Irwin et al.*, 2004; *Moore and Howard*, 2003], and thus may represent the waning, more evaporative, phase of a paleolake.

[54] The montmorillonite end-member is associated with crater materials in NW Ariadnes (Figure 11). Here a smaller crater lies within a larger crater, where the ejecta of the larger crater postdates the bright mounds on the floor of Ariadnes. Olivine is exposed on the rim and floor of the larger crater. Montmorillonite is exposed in the ejecta, walls and floor of the smaller crater. Its limited geographic distribution may indicate excavation of a smectite-rich layer by the small crater, or the production of smectite due to hydrothermal alteration associated with the impact itself.

3.2.4. Summary

[55] The superpixel/SMACC algorithm within the Hii-HAT software is applied to the analysis of CRISM FRT images in Ariadnes Chaos. The algorithm identifies a suite of geologically meaningful end-members and does so consistently across the images. The compositional mapping provided in Hii-HAT allows a quick examination of the distribution of the end-members that could be compared

to other image data sets for geological interpretation. This preliminary analysis shows the chaos mounds to include a complex assemblage of phyllosilicates and sulfates requiring both and perhaps alternating water-rich and evaporitic conditions. These minerals and their stratigraphy are consistent with deposition from a paleolake at the bottom of the Ariadnes basin. These materials were subsequently eroded into mounds and later covered by dark materials we suggest are volcanic. The emplacement of the dark materials may have dehydrated the mound materials where in contact.

4. Discussion

[56] The automated superpixel segmentation and end-member detection strategy outlined here performs with high accuracy in CRISM full-resolution images. The method correctly identifies each of the end-members labeled manually. Part of the success of this strategy is superpixel segmentation, which by averaging together spectrally similar adjacent pixels reduces the noise in the end-member spectra [*Thompson et al.*, 2010]. The superpixel segmentation is similar to a noise reduction step in CRISM analyses frequently reported in the literature, whereby the analyst manually selects and averages regions of spectrally similar pixels for noise reduction. Our automated approach requires few assumptions about the physical characteristics of the scene apart from spatial continuity of physical features. Representing the scene by small contiguous regions can better capture the physical layout of materials on the surface and facilitate automated identification of geologically meaningful spectral units.

[57] The unsupervised classification approach described here has several advantages appropriate for the analysis of planetary data sets. Because the surface materials are not known a priori, unsupervised classification strategies maximize the chances of identifying all end-members in a scene including materials that are not anticipated. This capability is critical for finding novel or isolated spectral classes. This approach is complimentary to supervised techniques like the CRISM summary products and may reduce analysis time in situations where supervised techniques give nonunique results. For example for image 98b2, the ROC curves demonstrate that some mineral classes are equally well represented by a number of CRISM summary products (Figure 3a), thus the analyst must examine each potential index independently to determine the type and distribution of a given spectral class. The superpixel strategy might reduce analysis time by delivering target end-members to the analyst directly.

[58] A potential disadvantage of the unsupervised approach is that because it by definition identifies the most spectrally anomalous materials in a scene, there is potential for it to miss common materials. For example in the M^3 data, the prescribed end-members do not contain examples of the most common materials in the scene, which are the numerous spectrally distinct regolith materials (e.g., Figures 10a, 10c, and 10e). Two factors may be contributing this nondetection result. First, since common materials comprise most of the data set they define and dominate the spectral average of the scene they are not statistically distinctive. This issue can be mitigated by expanding the search strategy to include a greater number of end-members for large scenes such as M^3. Also, the minimum superpixel size (20 pixels ~0.4 km^2) is much smaller than the scale of many of the spectral units in the scene, prioritizing the detection of small outcrops (e.g., the crater central peaks) at the expense of geographically larger spectral units (e.g., mare lava flows). Increasing the superpixel size may be a desired strategy to target spatially large units in some data sets. Thus some experimentation may be required by the user to optimize the number of requested end-members and superpixel size for a given data set. We find that for the CRISM FRT data, 10 end-members and minimum superpixel size of 50 (~0.02 km^2) appropriately captured all spectral units in the scene including spectrally neutral classes and multiple examples of various end-members (Figures 5 and 15).

[59] The automated superpixel segmentation and end-member detection method also characterizes the data specific to each scene, where relative spectral differences are maximized. This has the advantage of accommodating scene-specific noise or background materials. This was seen in CRSIM FRT images 3e12 and 3fb9, where the 1 μm absorption associated with olivine is present in the carbonate-rich spectra. The unsupervised scheme readily identifies this spectral mixture as an end-member in the scene. Mineral mixtures are undoubtedly present on planetary surfaces representing primary mineralogy or as contaminants; for example, instrument noise, bad weather (e.g., high aerosols), near ubiquitous ferric Martian dust, or local dust generated by soft minerals such as sulfates [e.g., *Bishop et al.*, 2009] are readily observed. The enhanced performance measured by the AUC statistic of the superpixel method over the CRISM summary products is likely due to the algorithm's ability to recognize end-members that are truer matches to target (often mixed) materials. This effect can be seen graphically in Figure 6, where the CRISM index detects the target mineral well, but not exclusively.

[60] For the CRISM images, the automated method end-members included spectrally neutral regions. While not optimal to control for in-column instrument noise, these do offer a way to quickly ratio spectra of interest to a neutral spectrum as was done in Figure 5. Ratioing is a technique reported in the literature to reduce noise in CRISM data and is often especially helpful to mitigate the effects of an imperfect atmospheric correction.

[61] While not directly relevant to accuracy, computation runtime is an important practical consideration. Currently the most onerous step is the median filter of the initial preprocessing step, which can take as long as 30 min on a modern desktop processor. Generating the superpixel representation takes less than 1 min for the CRISM FRT images. Subsequent steps are similarly fast thanks to the orders-of-magnitude reduction in data volume with the superpixel representation. The algorithms described in this work have been incorporated into the JPL Hii-HAT software suite as a plug-in to the IDL/ENVI analysis software. Individuals interested in using Hii-HAT are advised to visit http://hyperspectral.jpl.nasa.gov for further information.

5. Conclusions

[62] We present a new application of superpixel segmentation to the semiautomatic analysis of hyperspectral planetary data sets. The method readily identifies spectral end-members in CRISM and M^3 data that are geologically

reasonable and a good match to those identified by an expert, facilitating a comprehensive assessment of spectral class characteristics and distribution in a given scene. For CRISM FRT data, we find the algorithm performs as well as the state of the art analysis techniques. Furthermore, the superpixel/SMACC algorithm (1) examines the entire data set, which maximizes its ability to find minerals that are unanticipated and (2) directly recognizes end-member spectra which may reduce analysis time.

[63] The success of the technique is due to the following factors. Superpixel segmentation reduces scene-specific noise and promotes the discovery of spatially contiguous spectral classes that are consistent with geologic phenomena. The unsupervised classification step exploits the entire spectral data set to enhance the discovery of novel mineralogy. This method is also robust for the recognition of target minerals within mixed spectra typical of planetary surfaces.

[64] The technique was applied to the analysis of Ariadnes Chaos and consistently recognized several spectral classes including smectites, sulfates and mafic materials. Aqueous minerals are confined to the exposed centers of chaos mounds. Smectites and sulfate materials are mixed at the CRISM scale, consistent with precipitation under variable environmental (wet/dry) conditions in a restricted paleolake.

[65] This semiautomated technique is shown to be adaptable to a number of hyperspectral data sets, which is perhaps most relevant for data sets for which standard analysis techniques do not yet exist. Thus it holds promise for the rapid detection of spectral features of interest, reducing image analysis time and enabling more comprehensive investigations of hyperspectral data from across the solar system.

[66] **Acknowledgments.** We thank the CRISM team and Brown University for the use of the CRISM Analysis Tool (CAT) and their software contributions to the community. Detailed reviews of the manuscript are appreciated. Support from the NASA AMMOS Multimission Ground Systems and Services office is acknowledged. A portion of this research described in this paper was carried out at the Jet Propulsion Laboratory, California Institute of Technology, under a contract with NASA.

References

Adams, J. B. (1974), Visible and near-infrared diffuse reflectance spectra of pyroxenes as applied to remote sensing of solid objects in the solar system, *J. Geophys. Res.*, *79*, 4829–4836, doi:10.1029/JB079i032p04829.

Baldridge, A. M., S. J. Hook, J. K. Crowley, G. M. Marion, J. S. Kargel, J. L. Michalski, B. J. Thomson, C. R. de Souza Filho, N. T. Bridges, and A. J. Brown (2009), Contemporaneous deposition of phyllosilicates and sulfates: Using Australian acidic saline lake deposits to describe geochemical variability on Mars, *Geophys. Res. Lett.*, *36*, L19201, doi:10.1029/2009GL040069.

Bibring, J.-P., et al. (1989), Results from the ISM experiment, *Nature*, *341*, 591–593, doi:10.1038/341591a0.

Bishop, J. L., and E. Murad (2005), The visible and infrared spectral properties of jarosite and alunite, *Am. Mineral.*, *90*, 1100–1107, doi:10.2138/am.2005.1700.

Bishop, J., J. Madejova, P. Komadel, and H. Froschl (2002a), The influence of structural Fe, Al, and Mg on the infrared OH bands in spectra of dioctahedral smectites, *Clay Miner.*, *37*, 607–616, doi:10.1180/0009855023740063.

Bishop, J. L., E. Murad, and M. D. Dyar (2002b), The influence of octahedral and tetrahedral cation substitution on the structure of smectites and serpentines as observed through infrared spectroscopy, *Clay Miner.*, *37*, 617–628, doi:10.1180/0009855023740064.

Bishop, J. L., et al. (2008a), Phyllosilicate diversity and past aqueous activity revealed at Mawrth Vallis, Mars, *Science*, *321*, 830–833, doi:10.1126/science.1159699.

Bishop, J. L., M. D. Lane, M. D. Dyar, and A. J. Brown (2008b), Reflectance and emission spectroscopy of four groups of phyllosilicates: Smectites, kaolinite-serpentines, chlorites, and micas, *Clay Miner.*, *43*, 35–54, doi:10.1180/claymin.2008.043.1.03.

Bishop, J. L., et al. (2009), Mineralogy of Juventae Chasma: Sulfates in the light-toned mounds, mafic minerals in the bedrock, and hydrated silica and hydroxylated ferric sulfate on the plateau, *J. Geophys. Res.*, *114*, E00D09, doi:10.1029/2009JE003352.

Boardman, J. W., F. A. Kruse, and R. O. Green (1995), Mapping target signatures via partial unmixing of AVIRIS data, in *Summaries of the Fifth Annual JPL. Airborne Earth Science Workshop*, *JPL Publ.*, 95-1, 23–26.

Bunte, M., D. R. Thompson, R. Castaño, S. Chien, and R. Greeley (2011) Enabling Europa science through onboard feature detection in hyperspectral images, *Lunar Plan. Sci. Conf.*, *42*, Abstract 1888.

Chevrier, V., F. Poulet, and J.-P. Bibring (2007) Early geochemical environment of Mars as determined from thermodynamics of phyllosilicates, *Nature*, *448*, 60–63, doi:10.1038/nature05961.

Clark, R. N. (1999), Spectroscopy of rocks and minerals, and principles of spectroscopy, in *Manual of Remote Sensing*, vol. 3, *Remote Sensing for the Earth Sciences*, edited by A. N. Rencz, pp. 3–58, John Wiley, New York.

Clark, R. N., T. V. V. King, M. Klejwa, G. A. Swayze, and N. Vergo (1990), High spectral resolution reflectance spectroscopy of minerals, *J. Geophys. Res.*, *95*, 12,653–12,680, doi:10.1029/JB095iB08p12653.

Clark, R. N., G. A. Swayze, K. E. Livo, R. F. Kokaly, S. J. Sutley, J. B. Dalton, R. R. McDougal, and C. A. Gent (2003), Imaging spectroscopy: Earth and planetary remote sensing with the USGS Tetracorder and expert systems, *J. Geophys. Res.*, *108*(E12), 5131, doi:10.1029/2002JE001847.

Cloutis, E. A., et al. (2006), Detection and discrimination of sulfate minerals using reflectance spectroscopy, *Icarus*, *184*, 121–157, doi:10.1016/j.icarus.2006.04.003.

Dobigeon, N., S. Moussaoui, M. Coulon, J. Y. Tourneret, and A. O. Hero (2009), Joint Bayesian endmember extraction and linear unmixing for hyperspectral imagery, *IEEE Trans. Signal Process.*, *57*, 4355–4368, doi:10.1109/TSP.2009.2025797.

Ehlmann, B. L., et al. (2008) Orbital identification of carbonate-bearing rocks on Mars, *Science*, *322*, 1828–1832, doi:10.1126/science.1164759.

Ehlmann, B. L., et al. (2009), Identification of hydrated silicate minerals on Mars using MRO-CRISM: Geologic context near Nili Fossae and implications for aqueous alteration, *J. Geophys. Res.*, *114*, E00D08, doi:10.1029/2009JE003339.

Ehlmann, B. L., J. F. Mustard, and S. L. Murchie (2010), Geological setting of serpentine deposits on Mars, *Geophys. Res. Lett.*, *37*, L06201, doi:10.1029/2010GL042596.

Farrand, W. H., T. D. Glotch, J. W. Rice Jr., J. A. Hurowitz, and G. A. Swayze (2009), Discovery of jarosite within the Mawrth Vallis region of Mars: Implications for the geologic history of the region, *Icarus*, *204*, 478–488, doi:10.1016/j.icarus.2009.07.014.

Fawcett, T. (2006), An introduction to ROC analysis, *Pattern Recognit. Lett.*, *27*, 861–874, doi:10.1016/j.patrec.2005.10.010.

Felzenszwalb, P. F., and D. P. Huttenlocher (2004), Efficient graph-based image segmentation, *Int. J. Comput. Vis.*, *59*, 167–181, doi:10.1023/B:VISI.0000022288.19776.77.

Friedl, M. A., and C. E. Brodley (1997), Decision tree classification of land cover from remotely sensed data, *Remote Sens. Environ.*, *61*, 399–409, doi:10.1016/S0034-4257(97)00049-7.

Gilmore, M. S., J. P. Greenwood, and J. L. Bishop (2010) Sulfates in Iani Chaos, Mars, *Lunar Planet. Sci. Conf.*, *41*, Abstract 2374.

Glotch, T. D., and A. D. Rogers (2007), Evidence for aqueous deposition of hematite- and sulfate-rich light-toned layered deposits in Aureum and Iani Chaos, Mars, *J. Geophys. Res.*, *112*, E06001, doi:10.1029/2006JE002863.

Gruninger, J., A. J. Ratkowski, and M. L. Hoke (2004), The sequential maximum angle convex cone (SMACC) endmember model, *Proc. SPIE*, *5425*, doi:10.1117/12.543794.

Hogan, R. C. and T. L. Roush (2009) Mineral emittance spectra: Clustering and classification using self-organizing maps, in *IEEE 2009 Aerospace Conference*, pp. 1–7, IEEE, New York, doi:10.1109/AERO.2009.4839480.

Hunt, G. R., and J. W. Salisbury (1970), Visible and near-infrared spectra of minerals and rocks: 1. Silicate minerals, *Mod. Geol.*, *1*, 283–300.

Hunt, G. R., J. W. Salisbury, and C. J. Lenhoff (1971), Visible and near-infrared spectra of minerals and rocks. VI. Sulfides and sulfates, *Mod. Geol.*, *3*, 1–14.

Irwin, R. P., A. D. Howard, and T. A. Maxwell (2004), Geomorphology of Ma'adim Vallis, Mars, and associated paleolake basins, *J. Geophys. Res.*, *109*, E12009, doi:10.1029/2004JE002287.

Kruse, F. A., A. B. Lekoff, J. B. Boardman, K. B. Heidebrecht, A. T. Shapiro, P. J. Barloon, and A. F. H. Goetz (1993), The Spectral Image Processing System (SIPS)–Interactive visualization and analysis of imag-

ing spectrometer data, *Remote Sens. Environ.*, *44*, 145–163, doi:10.1016/0034-4257(93)90013-N.

Lichtenberg, K. A., et al. (2010), Stratigraphy of hydrated sulfates in the sedimentary deposits of Aram Chaos, Mars, *J. Geophys. Res.*, *115*, E00D17, doi:10.1029/2009JE003353.

Lundeen, S., S. McLaughlin, and R. Alanis (2010), Moon Mineralogy Mapper (M^3) data product software interface specification, version 9.4, JPL D-39032, Jet Propul. Lab., Pasadena, Calif. (Available at http://pds-imaging.jpl.nasa.gov/data/m3/CH1M3_0001/DOCUMENT/DPSIS.PDF.)

Marzo, G. A., T. L. Roush, A. Blanco, S. Fonti, and V. Orofino (2006), Cluster analysis of planetary remote sensing spectral data, *J. Geophys. Res.*, *111*, E03002, doi:10.1029/2005JE002532.

Marzo, G. A., T. L. Roush, A. Blanco, S. Fonti, and V. Orofino (2008), Statistical exploration and volume reduction of planetary remote sensing spectral data, *J. Geophys. Res.*, *113*, E12009, doi:10.1029/2008JE003219.

Marzo, G. A., T. L. Roush, and R. C. Hogan (2009), Automated classification of visible and infrared spectra using cluster analysis, *J. Geophys. Res.*, *114*, E08001, doi:10.1029/2008JE003250.

McGuire, P. C., et al. (2009), An improvement to the volcano-scan algorithm for atmospheric correction of CRISM and OMEGA spectral data, *Planet. Space Sci.*, *57*, 809–815, doi:10.1016/j.pss.2009.03.007.

McKeown, N. K., J. L. Bishop, E. Z. Noe Dobrea, B. L. Ehlmann, M. Parente, J. F. Mustard, S. L. Murchie, G. A. Swayze, J.-P. Bibring, and E. A. Silver (2009), Characterization of phyllosilicates observed in the central Mawrth Vallis region, Mars, their potential formational processes, and implications for past climate, *J. Geophys. Res.*, *114*, E00D10, doi:10.1029/2008JE003301.

Melgani, F., and L. Bruzzone (2004), Classification of hyperspectral remote sensing images with support vector machines, *IEEE Trans. Geosci. Remote Sens.*, *42*, 1778–1790, doi:10.1109/TGRS.2004.831865.

Milliken, R. E., et al. (2008), Opaline silica in young deposits on Mars, *Geology*, *36*, 847–850, doi:10.1130/G24967A.1.

Milliken, R. E., J. P. Grotzinger, and B. J. Thomson (2010), Paleoclimate of Mars as captured by the stratigraphic record in Gale Crater, *Geophys. Res. Lett.*, *37*, L04201, doi:10.1029/2009GL041870.

Moore, J. M., and A. D. Howard (2003) Ariadnes-Gorgonum knob fields of north-western Terra Sirenum, Mars, *Lunar Planet. Sci. Conf.*, *34*, Abstract 1402.

Murchie, S., et al. (2007a), Compact Reconnaissance Imaging Spectrometer for Mars (CRISM) on Mars Reconnaissance Orbiter (MRO), *J. Geophys. Res.*, *112*, E05S03, doi:10.1029/2006JE002682.

Murchie, S., E. Guinness, and S. Slavney (2007b), CRISM data product software interface specification, version 1.3.5, NASA Planet. Data Syst., Greenbelt, Md. (Available at http://ode.rsl.wustl.edu/mars/pagehelp/quickstartguide/documents/crism_dpsis.pdf.)

Murchie, S. L., et al. (2009a), Compact Reconnaissance Imaging Spectrometer for Mars investigation and data set from the Mars Reconnaissance Orbiter's primary science phase, *J. Geophys. Res.*, *114*, E00D07, doi:10.1029/2009JE003344.

Murchie, S. L., et al. (2009b), A synthesis of Martian aqueous mineralogy after 1 Mars year of observations from the Mars Reconnaissance Orbiter, *J. Geophys. Res.*, *114*, E00D06, doi:10.1029/2009JE003342.

Mustard, J. F., F. Poulet, A. Gendrin, J.-P. Bibring, Y. Langevin, B. Gondet, N. Mangold, G. Bellucci, and F. Altieri (2005), Olivine and pyroxene diversity in the crust of Mars, *Science*, *307*, 1594–1597, doi:10.1126/science.1109098.

Mustard, J. F., et al. (2008), Hydrated silicate minerals on Mars observed by the Mars Reconnaissance Orbiter CRISM instrument, *Nature*, *454*, 305–309, doi:10.1038/nature07097.

Mustard, J. F., B. L. Ehlmann, S. L. Murchie, F. Poulet, N. Mangold, J. W. Head, J.-P. Bibring, and L. H. Roach (2009), Composition, morphology and stratigraphy of Noachian crust around the Isidis Basin, *J. Geophys. Res.*, *114*, E00D12, doi:10.1029/2009JE003349.

Nascimento, J. M. P., and J. M. Bioucas-Dias (2005), Vertex component analysis: A fast algorithm to unmix hyperspectral data, *IEEE Trans. Geosci. Remote Sens.*, *43*, 898–910, doi:10.1109/TGRS.2005.844293.

Noe Dobrea, E. Z., F. Poulet, and M. C. Malin (2008), Correlations between hematite and sulfates in the chaotic terrain east of Valles Marineris, *Icarus*, *193*, 516–534, doi:10.1016/j.icarus.2007.06.029.

Parente, M. (2008), A new approach to denoising CRISM images, *Lunar Planet. Sci.*, *39*, Abstract 2528.

Parente, M. and J. L. Bishop (2010), Extracting endmember spectra from CRISM images: Comparison of new DiREX image transform technique with MNF, *Lunar Planet. Sci.*, *41*, Abstract 2633.

Parente, M., J. T. Clark, A. J. Brown, and J. L. Bishop (2010), End-to-end simulation and analytical model of remote-sensing systems: Application to CRISM, *IEEE Trans. Geosci. Remote Sens.*, *48*, 3877–3888, doi:10.1109/TGRS.2010.2050000.

Pelkey, S. M., et al. (2007), CRISM multispectral summary products: Parameterizing mineral diversity on Mars from reflectance, *J. Geophys. Res.*, *112*, E08S14, doi:10.1029/2006JE002831.

Pieters, C. M. (1993), Compositional diversity and stratigraphy of the lunar crust derived from reflectance spectroscopy, in *Remote Geochemical Analysis: Elemental and Mineralogical Composition*, edited by C. M. Pieters and P. A. J. Englert, pp. 309–339, Cambridge Univ. Press, Cambridge, U. K.

Plaza, A., P. Martinez, R. Perez, and J. Plaza (2002), Spatial/spectral endmember extraction by multidimensional morphological operations, *IEEE Trans. Geosci. Remote Sens.*, *40*, 2025–2041, doi:10.1109/TGRS.2002.802494.

Roach, L. H., J. F. Mustard, S. L. Murchie, J.-P. Bibring, F. Forget, K. W. Lewis, O. Aharonson, M. Vincendon, and J. L. Bishop (2009), Testing evidence of recent hydration state change in sulfates on Mars, *J. Geophys. Res.*, *114*, E00D02, doi:10.1029/2008JE003245.

Rogge, D. M., B. Rivard, J. Zhang, J. Harris, A. Sanchez, and J. Feng (2007), Integration of spatial-spectral Information for the improved extraction of endmembers, *Remote Sens. Environ.*, *110*, 287–303, doi:10.1016/j.rse.2007.02.019.

Roush, T. L., and R. C. Hogan (2007), Automated classification of visible and near-infrared spectra using self-organizing maps, in *2007 IEEE Aerospace Conference*, pp. 1–9, IEEE, New York, doi:10.1109/AERO.2007.352701.

Salvatore, M. R., J. F. Mustard, M. B. Wyatt, S. L. Murchie, and O. S. Barnouin-Jha (2009) Assessing the mineralogy of Acidalia Planitia, Mars, using near-infrared orbital spectroscopy, *Lunar Plan. Sci. Conf.*, *40*, Abstract 2050.

Swayze, G. A., et al. (2008), Discovery of the acid-sulfate mineral alunite in Terra Sirenum, Mars, using MRO CRISM: Possible evidence for acid-saline lacustrine deposits?, *Eos Trans. AGU*, *89*(53), Fall Meet. Suppl., Abstract P44A-04.

Thompson, D. R., L. Mandrake, M. S. Gilmore, and R. Castaño (2010), Superpixel endmember detection, *IEEE Trans. Geosci. Remote Sens.*, *48*, 4023–4033, doi:10.1109/TGRS.2010.2070802.

Tso, B., and P. M. Mather (2009), *Classification Methods for Remotely Sensed Data*, 2nd ed., CRC Press, Boca Raton, Fla., doi:10.1201/9781420090741.

Velde, B. (1995), *Clay Minerals: A Physico-Chemical Explanation of Their Occurrence*, Elsevier, New York.

Winter, M. E. (2004), A proof of the N-FINDR algorithm for the automated detection of endmembers in a hyperspectral image, *Proc. SPIE*, *5425*, 31–41, doi:10.1117/12.542854.

Wiseman, S. M., et al. (2008), Phyllosilicate and sulfate-hematite deposits within Miyamoto crater in southern Sinus Meridiani, Mars, *Geophys. Res. Lett.*, *35*, L19204, doi:10.1029/2008GL035363.

Wray, J. J., E. Z. Noe Dobrea, R. E. Arvidosn, S. M. Wiseman, S. W. Squyres, A. S. McEwen, J. F. Mustard, and S. L. Murchie (2009), Phyllosilicates and sulfates at Endeavour Crater, Meridiani Planum, Mars, *Geophys. Res. Lett.*, *36*, L21201, doi:10.1029/2009GL040734.

Wray, J. J., et al. (2011), Columbus crater and other possible groundwater-fed paleolakes of Terra Sirenum, Mars, *J. Geophys. Res.*, *116*, E01001, doi:10.1029/2010JE003694.

Zhang, J., B. Rivard, and D. M. Rogge (2008), The Successive Projection Algorithm (SPA), an algorithm with a spatial constraint for the automatic search of endmembers in hyperspectral data, *Sensors*, *8*, 1321–1342, doi:10.3390/s8021321.

Zortea, M., and A. Plaza (2009), Spatial preprocessing for endmember extraction, *IEEE Trans. Geosci. Remote Sens.*, *47*, 2679–2693, doi:10.1109/TGRS.2009.2014945.

L. J. Anderson and M. S. Gilmore, Department of Earth and Environmental Sciences, Wesleyan University, 265 Church St., Middletown, CT 06459, USA. (mgilmore@wesleyan.edu)

R. Castaño, N. Karamzadeh, L. Mandrake, and D. R. Thompson, Jet Propulsion Laboratory, California Institute of Technology, 4800 Oak Grove Dr., Pasadena, CA 91109, USA.